Delft University of Technology

Bachelor Thesis

Applied Physics

Temperature dependence of the attenuation and group velocity of ultrasonic waves in tungsten

by

A.R. de Reuver

to obtain the degree of Bachelor of Science
to be defended publicly on July 6^{th}, 2018 at 14:00

Student number: 4379578

Project duration: April 23^{th} to July 6^{th}

Thesis committee: Dr. ir. M. Rohde

Prof. dr. ir. N. de Jong

June 28, 2018

Abstract

This research is part of the SAMOFAR (Safety Assessment of the Molten Salt Fast Reactor) project. The final goal of SAMOFAR is to make nuclear reactors truly safe and sustainable. To obtain this goal the MSFR (Molten Salt Fast Reactor) was designed. To develop the MSFR it is essential to know the behaviour of the molten salt inside the reactor core (e.g. if the flow is laminar or turbulent). Thermodynamic properties, such as viscosity and density, are needed to determine this behavior. These thermodynamic properties cannot be derived using conventional experimental equipment due to the high temperature, radioactivity, and corrosiveness of the molten salt. A new presumed method to determine these thermodynamic properties makes use of ultrasonic waves traversing through a waveguide which is (partially) immersed in the molten salt. From the measurement of the ultrasonic wave velocity and attenuation considering two different immersion depths the viscosity and density of the molten salt can be determined. To test this approach an experimental prototype was made which will operate at room temperature. This research focuses on the difference the temperature will induce in the ultrasonic wave velocity and attenuation between room temperature and operational temperatures of an MSFR. The research was primarily done using simulations, with a reference experiment to couple the simulations to empirical results. Longitudinal, flexural, and shear wave modes at $2MHz$ were excited and traversed up and down a tungsten waveguide at seven different temperatures between $300K$ and $1500K$. The velocities of all wave modes were found to decrease over the whole temperature range with about 7%. The temperature dependency of the longitudinal and shear wave velocity was shown to be semi-linear, where the temperature dependency of the flexural wave velocity showed a more unpredictable behaviour. The attenuation of all wave modes generally increased over the considered temperature range, with longitudinal waves showing the biggest increase in attenuation (about 40%), followed by the flexural waves (increase of about 15%), while the shear waves only showed an increase in attenuation of 1%. Once more the temperature dependency of the attenuation of longitudinal and shear waves was shown to be semi-linear, where the flexural waves again showed a more unpredictable behaviour. Longitudinal and flexural waves showed a high attenuation overall ($\sim 50Np/m$) where the attenuation of shear waves was found to be around only $20Np/m$. Furthermore longitudinal waves were shown to experience extreme amounts of dispersion and interference of additional wave modes which makes qualitative derivations difficult. The dispersion and interference of additional wave modes found for flexural and shear waves was at acceptable levels, meaning the original wave front remained mostly intact and was clearly distinguishable. In general the shear waves seem to be the best fit for intended molten salt experiments as they show lower attenuation, are not problematically influenced by dispersion and additional wave modes, and show small temperature dependency. Although the effect of temperature on the shear waves is small this still needs to be considered if qualitative results are desired. For that reason follow up research in this field is recommended, making use of a denser distribution of considered temperatures especially around both room temperature and operational temperatures of an MSFR. If this temperature dependent behaviour of ultrasonic waves is completely characterized the prototype measurements at room temperature can be scaled up to measurements making use of actual molten salts, which will contribute to the final goal of SAMOFAR: to make nuclear energy safe, sustainable, and available for everybody.

CONTENTS

1 Introduction

As the world looks to decrease fossil fuel usage, the need for an alternative energy source has become more apparent. A lot of alternative energy sources have emerged in the past years (e.g solar, hydro, biomass, and wind) but non of these alternative energy sources are capable to meet the energy demand of the whole world right now. A breakthrough in renewable energy is needed, now more than ever. One of the options for renewable energy is nuclear energy, but generally speaking people do not like nuclear power after the meltdowns of the reactors in Chernobyl (1986), and more recently in Fukushima (2011), making those areas uninhabitable for hundreds of years. But what if nuclear energy can become safe, efficient, clean, and economically competitive? This would cause the paradigm to shift. In 2001 the Generation IV International Forum (GIF) was established, a forum for future systems of nuclear power that focuses on, among other things, sustainable energy with long-term availability, minimization of nuclear waste, economic advantages over alternative energy sources, and high safety. The MSFR (MSFR) is one of the six future designs. This research is part of the SAMOFAR (Safety Assessment of the Molten Salt Fast Reactor) project, an European research project which aims to obtain the goals set by the GIF.

1.1 The Molten salt fast reactor

The MSFR is a new design of nuclear reactors from which its origin dates back to the 1950s [1]. In MSFRs the fuel and the primary coolant consist of a molten salt mixture. The nuclear fuel, which consists of uranium ($\sim 20\%$), thorium ($\sim 1\%$), and plutonium ($\sim 3\%$), is dissolved in the coolant itself. Typically a molten salt mixture consists of two fissile isotopes, one fertile isotope, and one light-element compound. One of the contemplated molten salt mixtures is $LiF - ThF_4 - UF_4 - PuF_3$ [2]. LiF acts as a matrix within this quaternary salt. Figure 1 shows a schematic overview of a molten salt fast reactor. The heat of the nuclear reaction generated within the core of the reactor, using a primary salt as the fuel, is transferred to a secondary salt mixture via a heat exchanger. This secondary salt contains no fissile or fertile material and has thermodynamic properties that resemble those of the fuel. Often $FLiNaK$ is chosen for this secondary salt. The heat of the second loop is transferred again using a heat exchanger to a third loop containing water which drives a turbine, generating work, and thus energy.

In comparison with conventional nuclear reactors, the MSFR operates at higher temperatures ($\sim 1000K$) and low pressure ($\sim 1bar$). In Figure 2 a result of one of my previous works in this field can be seen showing the ternary phase diagram, as studied thoroughly already (summarized by Grimes [4]), of a possible molten salt: $NaF - LiF - PuF_3$. The two eutectic points, the points at which compositions the melting temperature of the salt is the lowest, are shown to be $980K$ and $897K$, which give an indication of the operating temperature of such an MSFR.

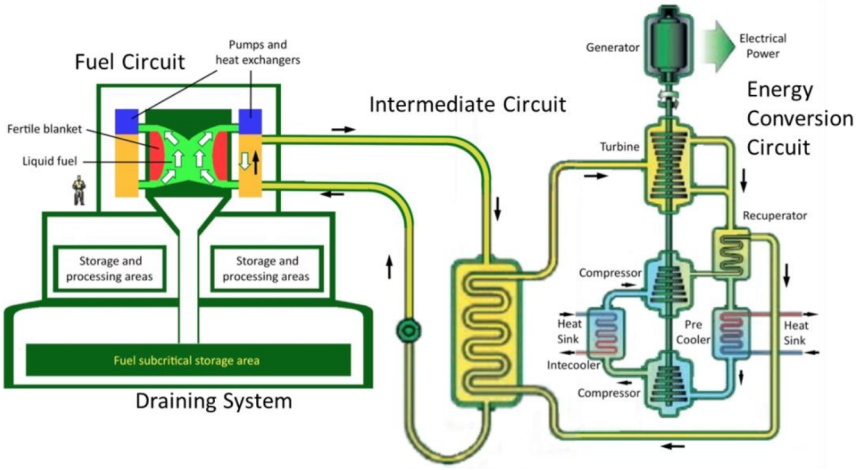

Figure 1: A schematic overview of the molten salt fast reactor [3].

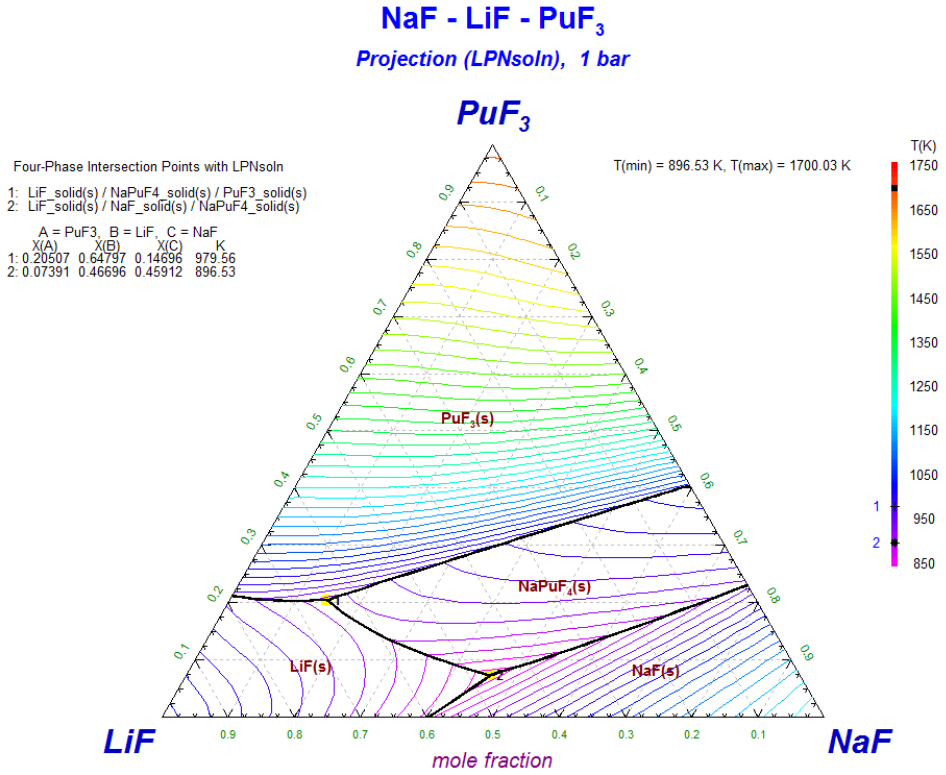

Figure 2: The ternary phase diagram of $NaF - LiF - PuF_3$.

The safety of the MSFR design is mainly due to the negative temperature coefficient of the molten salt, the freeze plug, and the operating conditions. The negative temperature coefficient slows down the reaction at higher temperatures by thermally expanding the salt, lowering the density of reactive compounds. The freeze plug will melt when the reactor becomes too hot resulting in a complete drainage of the reactor core, stopping all reactions. The operating conditions (approximately atmospheric pressure and very high temperatures) make sure that a breach of the reactor wall does not cause an explosion and if the molten salt were to leak out it would immediately solidify, preventing it from spreading.

1.2 Thermodynamic properties and ultrasonic wave measurements

The thermodynamic properties (e.g. density and viscosity) at operating conditions of the molten salt are interesting as they ultimately decide the ideal molten salt for a particular reactor, and at which operating conditions such a reactor needs to run. The density and viscosity appear in the Reynolds number which determines if a flow is turbulent or laminar, which influences the behaviour of the molten salt inside the reactor core. However, the determination of these thermodynamic properties is problematic. Conventional measurement instruments fail to operate at high temperatures ($\sim 1000K$) and highly corrosive and radioactive environments. Thus a new way to determine these thermodynamic properties needs to be explored. One of the possible approaches is to use ultrasonic wave measurements, extensively investigated by Cegla [5] [6] [7]. This non-destructive method pulses short ultrasonic waves at high frequencies (MHz range) through a waveguide which is partially immersed in the molten salt fluid. A piezo-electric transducer is placed on top of the wave guide, and thus physically distanced from the molten salt, eliminating the radioactive, corrosive, and high temperature induced problems. A piezo-electric transducer cannot operate at temperatures exceeding its Curie temperature as it will become depolarized, and high temperature operative transducers are not yet available, as stated by Stevenson et al. [8]. The distancing of the transducer from the molten salt allows the transducer to remain at cool temperatures, while the molten salt is around $1000K$. This causes a temperature gradient within the waveguide to appear.

Due to the wave propagating through the waveguide while the waveguide is (partially) immersed in the molten salt, properties of the molten salt can be retrieved from the measured echoes of the wave. Cegla has derived that the density and viscosity of the molten salt (or any fluid considered) can be deducted simultaneously using the attenuation and velocity of the ultrasonic wave. By doing different experiments with differing immersion depths the measurements of the attenuation and the velocity of the wave can be used to derive the viscosity and density of the molten salt, which, as stated before, cannot be measured directly.

1.3 Previous research

The aim of present research is to perform these measurements on a test set up at room temperature using another fluid (e.g. water or glycerol), instead of a molten salt (which is not a liquid at room temperature anyway). Previous research has been done on the different wave modes inside the waveguide [9] and the influence of tapering the waveguide [10]. Extensive research is currently done on the wave modes that get excited at the liquid-solid interface [11] [12] and the derivation of the viscosity and density [13] as stated by Cegla. The aim of this ongoing research is to develop a working prototype to eventually implement this method to derive the thermodynamic properties of the molten salt in a non-destructive manner. The desired prototype is shown in Figure 3.

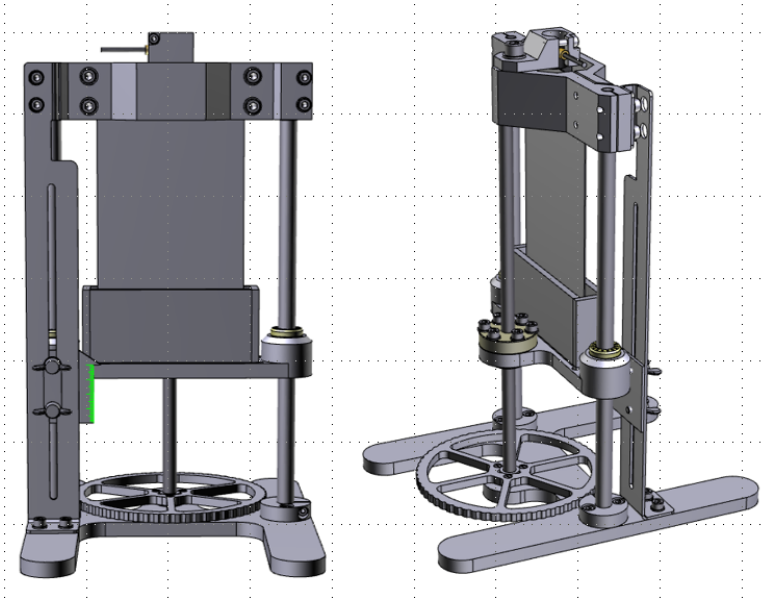

Figure 3: The desired prototype for the viscosity and density determination. The suspended plate acts as a waveguide which is semi-immersed in a fluid present in the container. At the top a piezo-electric transducer is placed [11].

1.4 Research goals

This research is part of the SAMOFAR project. The grand objective of SAMOFAR is to deliver a breakthrough in nuclear safety and nuclear waste management by showing proof of the safety and sustainability of the MSFR. A contribution to this project is the investigation of the behaviour of molten salt inside an MSFR. As stated before, the viscosity and density are needed for such research, which is the aim of the measurements of the attenuation and wave velocity using the previously mentioned prototype. If these measurements show promising results such experiments will be performed using molten salts at operating conditions of an MSFR. However, the prototype experiments are done at room temperature, and just like almost all physical properties, the attenuation and wave velocity are temperature dependent. The temperature dependency of these properties could have a big influence on the switch from the prototype to molten salt measurements. The aim of this research is to investigate the temperature dependence of the attenuation and wave velocities of different wave modes inside a waveguide. Thus far, very little research has been done on this particular subject. The research will be done using simulations with COMSOL Multiphysics [14] and post-processing with MATLAB [15]. A reference experiment will couple the simulations to the real world.

2 Theory

In this chapter the theory behind the research is covered. The basics of advanced wave propagation and continuum mechanics are briefly touched upon alongside with the approximations made in this research.

2.1 Primary wave modes

Within this research three wave modes are primarily investigated, namely: longitudinal, flexural, and shear waves. All three of the wave modes are displayed in Figure 4.

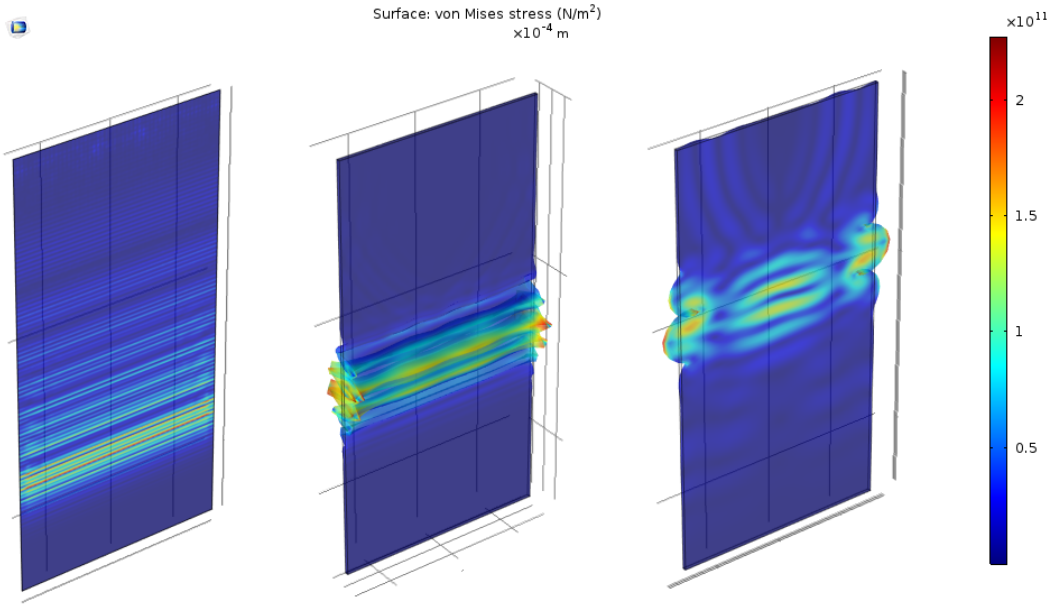

Figure 4: The three considered wave modes. In the leftmost waveguide a longitudinal wave is propagating, in the middle waveguide a flexural wave mode is shown, and in the rightmost waveguide a shear wave propagates. The propagation direction for all wave modes is downwards. The deformation of the material is displayed in exaggerated form. The surface plot colours represent the von Mises stress, which will be covered in chapter *2.3: Continuum mechanics*.

Longitudinal waves

Longitudinal waves, S0 waves, sound waves, pressure-Lamb waves (P-Lamb waves), acoustic waves, dilatational waves, or just P-waves, are waves which vibrate in the direction of propagation. An example of these waves are ordinary sound waves which humans can hear. A particle experiencing the passing of a longitudinal wave only moves "up and down", if the up and down direction are chosen in the propagation direction of the wave.

Flexural waves

Flexural waves, A0 waves, S-Lamb waves, transverse waves, or water waves are surface waves that vibrate in a direction perpendicular to their propagation. Strictly speaking water waves are a combination of longitudinal and flexural waves but the latter part is dominant. A particle experiencing the passing of a flexural wave emits a circular motion around its equilibrium position, passing its movement on to its neighbour, propagating the wave mode. This is clarified in Figure 5 [12]. A common example of these waves are everyday water waves in the seas and oceans. A common misconception about these kind of waves is that a water particle moves around the whole ocean, where in fact it actually remains in place and carries out a circular (or elliptical) motion.

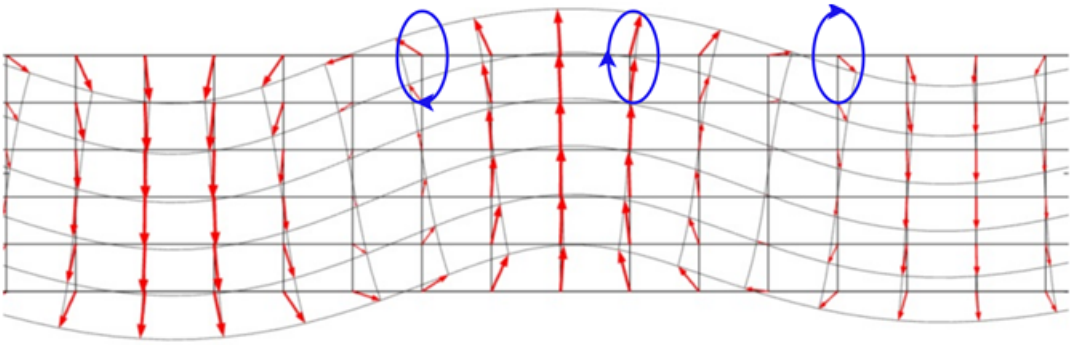

Figure 5: A flexural wave propagating in a plate-like waveguide. Of three particles their trajectory is denoted with the blue circles. The deformation of the waveguide is exaggerated [12].

Shear waves

Shear waves, SH0 waves, shear horizontal waves, secondary waves, elastic S-waves, or just S-waves, are the second kind of surface waves that vibrate in the other direction perpendicular to the propagation direction than the flexural waves (as shown in Figure 4). If a plate-like waveguide is considered shear waves have displacements along the narrow side of the plate, where flexural waves displace the wide side of the plate. The basic underlying physics for both flexural and shear waves is similar, but the wave properties can differ. Shear waves attenuate way less than flexural waves, which can intuitively be explained by the fact that shear waves displace "less waveguide" whilst propagating as compared to flexural waves. An example of shear waves are the shear waves inside the crust of the earth that seismic stations pick up (along with P-waves) to determine the epicentre of an earthquake.

2.2 Additional wave modes

Waves inside a waveguide show a shapeshifting behaviour. Due to interactions with the boundaries of the solid waveguide the wave modes, which propagate in a rotational (flexural and shear) and longitudinal manner, can convert into one another. This phenomenon is called mode conversion. Such converted wave modes are often called trailing or spurious

echoes. As Froeling [9] has shown these echoes can be categorized into three different types: head waves, longitudinal wavefronts, and radiated edge waves. These trailing echoes are clarified in Figure 6.

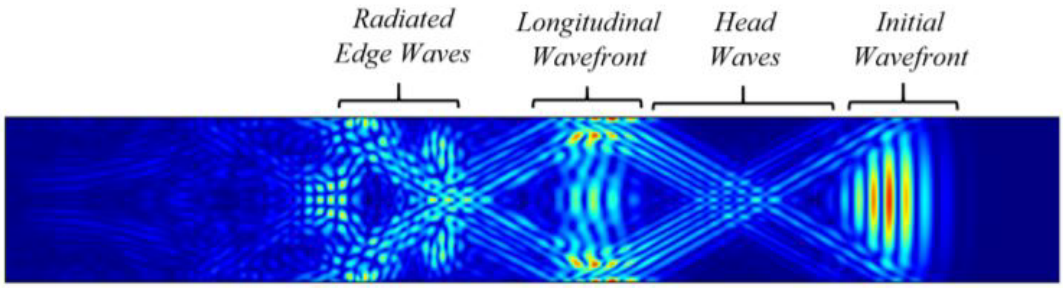

Figure 6: The different wave modes inside a wave guide, in this case created by the interaction of an initial longitudinal wavefront with the boundaries. The surface plot colours denote the von Mises stress, which will be covered in chapter *2.3: Continuum mechanics*.

Another additional wave mode is the Scholte wave mode (or Stonely-Scholte wave mode). These waves are created at the solid-liquid interface and are of great importance in the intended density and viscosity calculations of the molten salt. These waves are surface waves propagating at this particular interface. Most of the energy of the Scholte waves is carried inside the fluid. The Scholte wave is attenuated, (partially) due to the viscosity of the fluid, in its propagation direction and excites longitudinal waves inside the fluid. These longitudinal waves decay exponentially away from the interface, and thus only exist close to this interface. Theoretical understanding of the Scholte waves can be found in Rose [16]. In the desired prototype experiment quasi-Scholte waves are encountered instead of Scholte waves. In many dispersion diagrams frequency thickness is used on the $x-$axis instead of just frequency or thickness. This is done because those two quantities can not be seen individually from each other. Frequency and wavelength are related with each other via

$$\lambda = \frac{c}{f}, \tag{1}$$

in which λ is the wavelength, c is the velocity of the wave, and f is the frequency. If the frequency becomes higher, the wavelength becomes shorter. For a given waveguide thickness more wave modes can be excited for higher frequencies. In other words: the same waveguide "feels" thicker for higher frequency wave modes than for lower frequency wave modes. For this reason frequency and thickness need to be considered in combination with each other. Quasi-Scholte waves are an approximation of Scholte waves for non-infinite frequency thicknesses, and as a plate-like waveguide has a finite thickness and finite frequencies are used, the waves considered in these experiments are quasi-Scholte waves. In the limit of infinite frequency thicknesses the quasi-Scholte waves will become Scholte waves.

2.3 Continuum mechanics

To understand the propagation and behaviour of ultrasonic waves a fundamental understanding of continuum mechanics is necessary.

Stress

Stress is the force that particles exert on each other per area. This can happen in two directions: normal to the plane (which is comparable to pressure for fluids and gasses) or perpendicular to the plane. These two stresses are called normal and shear stress and are depicted in Figure 7.

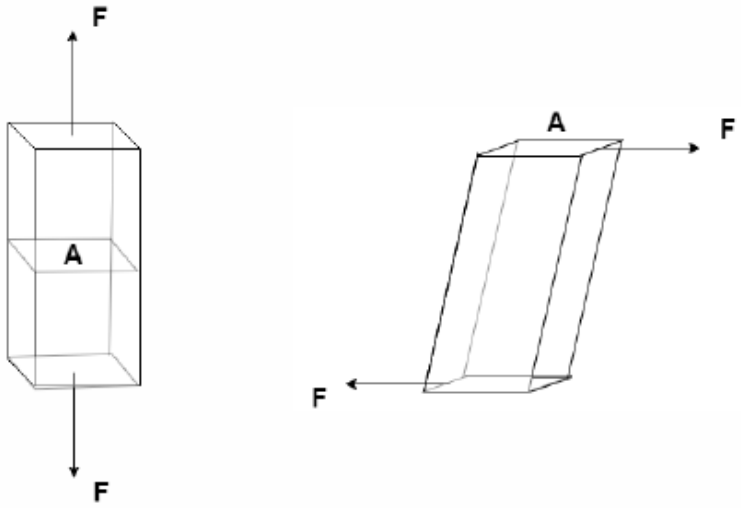

Figure 7: The two different stresses. On the left normal stress is shown with its force components normal to the plane and on the right shear stress is shown with its force components perpendicular to the plane.

Theses forces (F) shown in Figure 7, working on either side of the area (A), must be equal as the massless plane (a plane is two-dimensional and therefore massless) cannot experience an infinite acceleration (which would follow from Newtons second law of motion). Since a plane is considered, volume forces (e.g. gravity) can be disregarded. Considering every normal and shear stress component acting on a volume the total stress tensor could be constructed:

$$\overrightarrow{\overrightarrow{T}} = \begin{bmatrix} \sigma_{xx} & \sigma_{xy} & \sigma_{xz} \\ \sigma_{yx} & \sigma_{yy} & \sigma_{yz} \\ \sigma_{zx} & \sigma_{zy} & \sigma_{zz} \end{bmatrix}, \tag{2}$$

in which σ stands for stress in a particular direction. The term σ_{ii} denotes normal stresses and σ_{ij} (where $i \neq j$) denotes shear stresses. The tensor is symmetric as the stresses σ_{ij} and σ_{ji} need to be equal to prevent infinite acceleration. This tensor is known as the Cauchy stress tensor. This Cauchy stress tensor is shown working on a volume in Figure 8 [14].

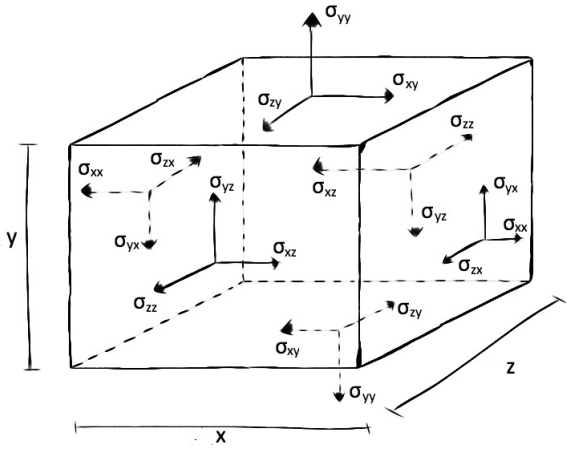

Figure 8: The Cauchy stress tensor working on a cubic volume.

The von Mises stress is a scalar value that can be computed from the Cauchy stress tensor:

$$\sigma_v = \sqrt{\frac{(\sigma_{xx} - \sigma_{yy})^2 + (\sigma_{yy} - \sigma_{zz})^2 + (\sigma_{zz} - \sigma_{xx})^2 + 6(\sigma_{xy}^2 + \sigma_{yz}^2 + \sigma_{zx}^2)}{2}}, \tag{3}$$

in which σ_v denotes the von Mises stress. It is defined as the maximum distortion energy criterion. A material starts yielding when the von Mises stress reaches the yield strength of the material (which is another material specific property). It is convenient to look at surface plots of the von Mises stress as it immediately becomes clear where the local stress field has relative minima and maxima.

Strain

Strain is a measurement of deformation of the material. Strain considers the deformation relative to the equilibrium position and is therefore a unitless quantity. Just like stress, strain can happen in the direction of the applied force, which is called normal strain, and in a direction perpendicular to the applied force, which is called shear strain. Unsurprisingly the Cauchy strain tensor is very similar to the Cauchy stress tensor:

$$\overrightarrow{\overrightarrow{E}} = \begin{bmatrix} \epsilon_{xx} & \epsilon_{xy} & \epsilon_{xz} \\ \epsilon_{yx} & \epsilon_{yy} & \epsilon_{yz} \\ \epsilon_{zx} & \epsilon_{zy} & \epsilon_{zz} \end{bmatrix}, \tag{4}$$

where ϵ stands for the strain component in a particular direction. This tensor is symmetric as well. Strain induces stress and vice versa. Several moduli exist to describe the behaviour of a material up to a certain amount of stress. The bulk Modulus K describes the the resistance to compression, the shear modulus G describes the response of a material to shear stress, and Youngs modulus E describes a response of a material to linear stress. These three moduli contain enough information to describe the behaviour of isotropic (which means that the material behaves uniformly in all orientations) materials. Describing the behaviour

of a material with the previously mentioned moduli works well up until the yielding point of the material. After that point the elasticity curves are not linear anymore and a tangent modulus function needs to be incorporated describing the behaviour of the material in the post-yielding regime.

In this research the behaviour of the wave will be investigated by looking at the second Piola-Kirchoff stress tensor:

$$\overrightarrow{\overrightarrow{S}} = J \overrightarrow{\overrightarrow{F}}^{-1} \overrightarrow{\overrightarrow{T}} \overrightarrow{\overrightarrow{F}}^{-T}, \tag{5}$$

where the $F-$tensor denotes the deformation gradient tensor, which is related to the Cauchy strain tensor, and J is the determinant of the deformation gradient tensor. T denotes the transpose operator and just like the strain and stress tensors, the $S-$tensor is symmetric. Looking at the second Piola-Kirchoff stress tensor holds several advantages as, for a deforming material, it holds all relevant information needed and minimizes computational power [14].

Additional mechanical engineering

If a material warms up it starts to show thermal expansion. A thermal expansion function is needed to describe this behaviour. If a material is not assumed to be perfectly plastic (or perfectly elastic) hardening functions are needed to describe the behaviour of the shear stress on a material after it yields. A hardening function is a function dependent on both temperature and strain. Initial yield stress is defined as the stress experienced due to a strain of 0.2%. The hardening function, initial yield stress, and the three previously mentioned moduli define the whole strain stress curve of a material. This curve is linear up until the yielding point.

2.4 Wave equations

Longitudinal waves are excited by a perturbation in a medium, inducing a local pressure difference (or normal stress). This stress induces strain and moves the medium, and this movement propagates through the medium as a wave. This wave can easily be created using a piezo-electric transducer. The three-dimensional wave equation of longitudinal waves can be derived using Hooke's law of deformation and Newton's equations of motion [16]:

$$\triangle \vec{p}(t) - \frac{1}{c^2} \frac{\partial^2 \vec{p}(t)}{\partial t^2} = 0, \tag{6}$$

where $\vec{p}(t)$ is the time dependent three-dimensional pressure field and c is the speed of the longitudinal wave in the medium, which is defined as:

$$c^2 = \frac{1}{\rho \kappa}, \tag{7}$$

in which ρ is the density and κ is the compressibility of the medium. $\triangle$ is the notation used for the Laplacian. Equation 6 holds the assumption that the considered medium is inviscid and can be expanded to include viscosity. The equation then becomes:

$$\triangle \vec{p}(t) - \frac{1}{c^2}\frac{\partial^2 \vec{p}(t)}{\partial t^2} + \frac{4\mu}{3}\frac{\partial \triangle \vec{p}(t)}{\partial t} = 0, \tag{8}$$

where μ denotes the viscosity of the medium considered. Equation 8 does not only hold for longitudinal waves, but also for rotational waves [16], which can either be flexural or shear waves depending on the considered geometry. Assuming low viscosities, which is a reasonable assumption as liquid steel has a viscosity in the $mPas$ range as shown by Korolczuk-Hejnak et al. [17], and making use of a Taylor expansion Cegla has shown that the velocity and attenuation of longitudinal and rotational wave modes are given by:

$$c_l = \sqrt{\frac{Re\{K\}}{\rho}}, \tag{9}$$

$$\alpha_l = \frac{4\pi\omega\mu}{3Re\{K\}}, \tag{10}$$

$$c_r = \sqrt{\frac{2\omega\mu}{\rho}}, \tag{11}$$

and

$$\alpha_r = 2\pi, \tag{12}$$

respectively, where $Re\{K\}$ denotes the real part of the bulk modulus of the fluid, ω is the angular frequency of the excited wave mode, and the subscripts l and r denote the longitudinal and rotational wave modes respectively. The α stands for the attenuation in neper per wavelength. Cegla has also shown that for rotational waves propagating in a waveguide another relation for the attenuation holds well for small frequency thicknesses (smaller than $2MHz$ [5] [16]):

$$\alpha_r = \sqrt{\frac{\rho_f \omega\mu}{2\rho_s G h^2}}, \tag{13}$$

in which G denotes the shear modulus of the waveguide, h denotes the thickness of the waveguide, and the subscripts f ans s denote the fluid and the solid respectively. With these formulae (9, 10, 11, 12, and 13), ultimately, the density and viscosity derivations will be done.

2.5 Wave behaviour and dispersion

Waves in a waveguide behave differently than waves inside a bulk material. Key differences are listed in Table 1 [16].

Table 1: Comparison between waves in bulk material and in waveguides

	Waveguide	**Bulk material**
Phase velocity	Function of frequency	Constant
Group velocity	Not equal to phase velocity	Same as phase velocity
Pulse shape	Disperse	Non-disperse

The group velocity is the velocity of the overall shape of the wave package, or the envelope of the wave. Mathematically this is given as:

$$c_g = \frac{\partial \omega}{\partial k}, \tag{14}$$

with c, ω, and k the velocity, angular frequency, and wave number respectively. The phase velocity is the velocity of the individual peaks (every individual frequency) within the wave package. Mathematically this differs subtly from the group velocity as it is not given as the partial derivative but as:

$$c_p = \frac{\omega}{k}, \tag{15}$$

where the subscripts g and p stand for group and phase. As shown in Table 1 the phase and group velocities differ from one another within waveguides. One can imagine that, if that is the case, an original wave package gets distorted and spreads out over time. This causes a separation of different frequencies within a wave mode. This phenomenon is called dispersion and an example is shown in Figure 9 [16].

Dispersion is a generally unwanted but unavoidable phenomenon as it makes the study and data analysis of waves more complicated, as one can not look at individual peaks anymore, but the whole wave package needs to be considered. In Figure 10 two flexural waves can be seen, one of which is undispersed (left) and one of which has experienced dispersion (right), as comparable to Figure 9.

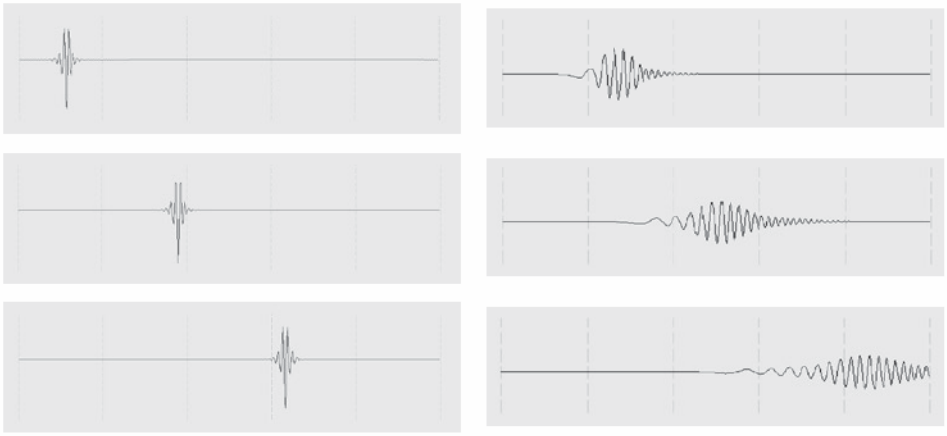

Figure 9: On the left a non-disperse wave is shown propagating at three different times. The shape of the wave package remains constant. On the right a disperse wave is shown propagating at three different times. Because of the difference between the group and phase velocity the wave package gets deformed and spreads out over time.

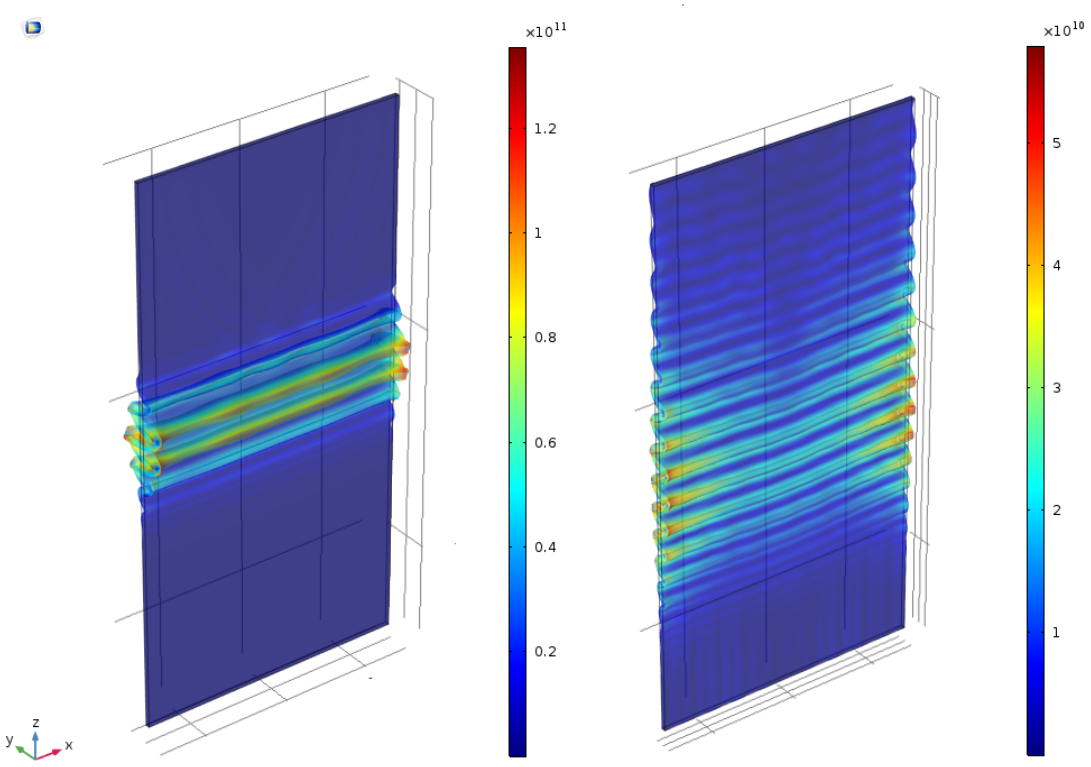

Figure 10: The dispersion of a flexural wave mode. At the left a flexural wave mode at an early point in time can be seen which shows virtually no dispersion. At the right a flexural wave mode can be seen at a later point in time, where disperse effects have occured, the wave is more spread out and less intense. The displacement and deformation are exaggerated. The colours of the surface plot denote the von Mises stress in Nm^{-2}.

2.6 Velocity and attenuation calculations

In this research the velocity and attenuation are derived for different temperatures. Because of dispersion and mode conversion the velocity calculations are not as straightforward as they seem. The velocity calculated is the group velocity and will be calculated using the maxima of the envelopes of wave packages. This velocity is defined as:

$$c = \frac{\Delta z}{\Delta t}, \tag{16}$$

wherein Δz is the traversed distance of the wave package and Δt is the time difference between the two peaks of the envelope of the wave. This envelope function is created by the quadratic sum of the original signal and its Hilbert transform. Theoretical understanding of these envelopes can be found in Oppenheim et al. [18] and the connection back to wave packages in Rose [16]. An example of such an envelope is given in Figure 11.

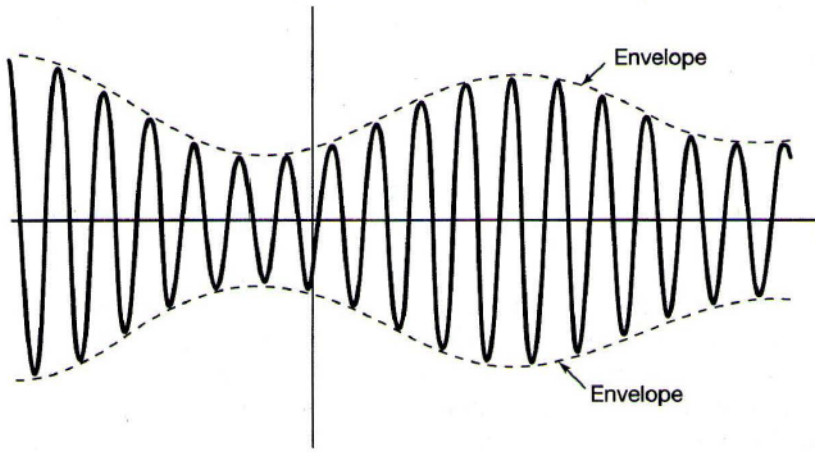

Figure 11: An analytic envelope created over an original signal. The negative envelope is plotted as well.

The attenuation can be derived in a plethora of ways. Attenuation is the decrease of flux intensity of a signal which propagates through a medium. Within wave mechanics attenuation is mainly defined as the logarithmic ratio between two amplitudes over a distance, given either in decibels (dB) or neper (Np) per meter ($1Np \approx 8.7dB$). Some attenuation calculation methods also incorporate the length of a pulse alongside with its maximum, which results in a sort of energy attenuation for disperse wave packages. In this research the attenuation is purely the attenuation of the intensity of the wave. This is the same approach as chosen in Schuringa [13] as this research also serves as the follow up research considering the work of Schuringa. This attenuation is defined as:

$$\alpha = \frac{ln(A) - ln(B)}{L}, \tag{17}$$

where A and B are the maxima of the envelope of a first and second pulse respectively. L denotes the traversed pathlength of the wave between the two considered peaks. A method

to evaluate the attenuation using three pulses exists as well which is more precise, as shown in Papadikis et al. [19]. However the computation power needed for such a simulation falls beyond the scope of this research as longer time periods need to be considered for a wave to return thrice instead of twice.

2.7 Material properties

For this research tungsten (W) is used. Tungsten is chosen as it will be a strong candidate for the intended waveguide in the molten salt experiments because of its robustness. It has the highest melting point of all known elements (around $3695K$) and is fairly resistant to corrossivity. The properties of tungsten are taken as stated in Binkele [20]. The termal expansion function and the tangent coefficient of thermal expansion (which is the derivative of the thermal expansion function with respect to temperature) are taken from the research of Hidnert and Sweeney [21]. The hardening function, initial yield stress, and tangent modulus (which is the derivative of the hardening function with respect to temperature) are taken from the strain stress curve for tungsten of the Zerilli-Armstrong model defined in Yadav and Ramesh [22]. Since tungsten is a metal, it is isotropic. For the greater part of this research thermal expansion is ignored as at a temperature of $1000K$ the thermal expansion causes an expansion of less than 0.001%. Also, for the greater part of the research the material is assumed to be perfectly plastic (or perfectly elastic). This assumption is verified by the fact that tungsten at $1000K$ only starts to yield at stresses greater than $500MNm^{-2}$, which are stresses not experienced with a simple piezo-electric transducer. Furthermore gravity was not considered as ultrasonic waves hardly get influenced by gravity. Lastly, for computation time purposes, the simulations were done in a vacuum. This is justified by the fact that air is one thousand times less dense as water and the immersion in water only influences the attenuation by a factor 1.5 [13].

3 Simulation and experimental method

The ultimate goal of the main research, where this subresearch is a part of, is to determine the viscosity and density of a molten salt. With this viscosity and density, among other things, the Reynolds number can be determined which defines if a fluid is behaving turbulent or laminar. For viscosity determination various techniques already exist. One of those techniques consists of letting an object pass through a viscous fluid and determining its drag force on the object, which is dependent on the viscosity of the fluid for Reynolds numbers smaller than one, as stated by Janssen and Warmoeskerken [23]. Another way is to measure the friction on a fluid as it flows through a tube. The friction is dependent on the viscosity of said fluid up until Reynolds numbers in the order of 10^5 [23]. Apart from fluid mechanical measurements similar measurements can be done considering heat or mass transfer [23].

However these measurements are problematic with molten salts as molten salts are radioactive, corrosive, and extremely hot. Because of this reason only a small amount of the molten salt can be used for measurements which makes the above mentioned techniques impractical. The method desired is the one already explained in chapters *1.2: Thermodynamic properties and ultrasonic wave measurements* and *2.4: Wave equations*, making use of ultrasonic waves. The waveguide (in this case made out of tungsten) can withstand the corrosive environment and high temperatures, and only a small fraction of molten salt should be sufficient for the determination of the density and viscosity of the molten salt. An additional advantage is the fact that the density and viscosity can be determined simultaneously using the same data.

3.1 Simulation set up

The simulations in this research were done using COMSOL Multiphysics 5.3 [14]. COMSOL Multiphysics is a finite element analysis solver and simulation software. To carry out a simulation the model environment needs to be set up, a geometric object needs to be defined, material properties need to be specified, the boundary conditions need to be defined, and the voxel (or mesh) size needs to be chosen before the simulation can be run. Afterwards post-processing of the data is done in MATLAB R2018a [15]. To investigate the temperature dependence of the attenuation and velocity of ultrasonic waves inside the waveguide every simulation was run at seven different constant temperatures between $300K$ and $1500K$ in steps of $200K$. In the desired molten salt experiments a temperature gradient is present instead of a constant temperature all around, but this temperature gradient causes the simulations to be more complex. Combining this with the fact that the basics of this temperature dependent behaviour are not widely understood validates to, as a start, only consider constant temperatures, to lay a foundation for follow up research.

The model environment

For the model environment used to simulate ultrasonic waves in a plate-like waveguide made out of tungsten the *Solid Mechanics*^{TM} module is used which is a submodule of the *Structural Mechanics*^{TM} module, used primarily for mechanical analyses. This analysis is done by approximating the Navier-Stokes equations for a solid.

Geometric objects

The plate-like waveguide is built as a geometric object with the correct dimensions. For the longitudinal and flexural waves a small waveguide is used as the computation time and file size of the solved simulation increase exponentially with waveguide size. The waveguide was obligated to have a depth (or thickness) of less than $1mm$ as the frequency thickness could not exceed $2MHzmm$ for minimal creation of additional unwanted wave modes [16]. The plate-like waveguide for the shear waves needs to have greater dimensions than the waveguide for the other two wave modes to obtain a certain frequency wideness to ensure "clean" shear wave propagation without distortion by additional wave modes, comparable with the earlier mentioned problems a too big frequency thickness would introduce. The dimensions of the "small" waveguide are 120 by 60 by $0.1\ mm$, and for the "big" waveguide the dimensions are 400 by 200 by $0.1\ mm$ (length $\times$ width $\times$ depth). The "big" waveguide can be seen in Figure 12.

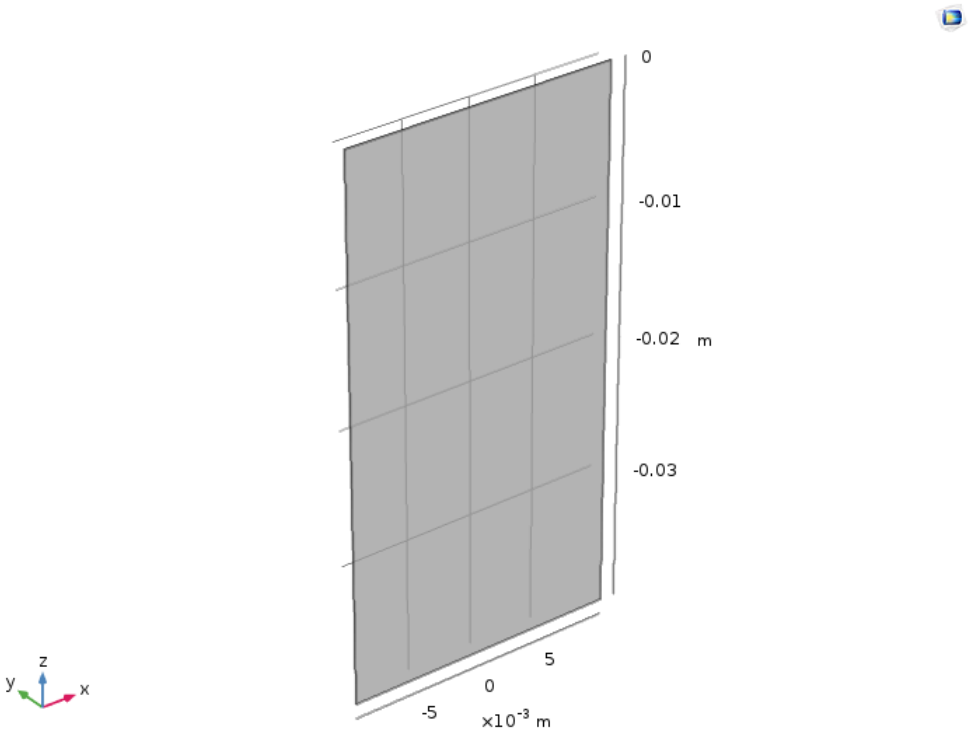

Figure 12: The "big" plate-like waveguide created. The dimensions and the coordinate system are shown. The depth is not indicated as it is too small in comparison with the width and the length. The depth equals $0.1mm$

Material properties

The material of the plate-like waveguide is specified within COMSOL Multiphysics. In this research tungsten was chosen with its material properties as stated by Binkele [20] and additional stress strain and thermal expansion curves as stated by Tadav and Ramesh [22] and Hidnert and Sweeney [21] respectively. As stated before, tungsten is isotropic and for most simulations it will be approximated as perfectly plastic and thermally inexpandable. With the thermal inexpandability only the actual physical deformation of a material is disregarded. A decrease in density, which is also a result of thermal expansion, is still considered as the density is an important factor in the wave velocity and attenuation (see equations 9, 10, 11, and 13).

Boundary conditions

For a simulation to be successful valid boundary conditions need to be applied. For the creation of the ultrasonic wave one of the boundaries (see Figure 13) is set to have a predescribed displacement.

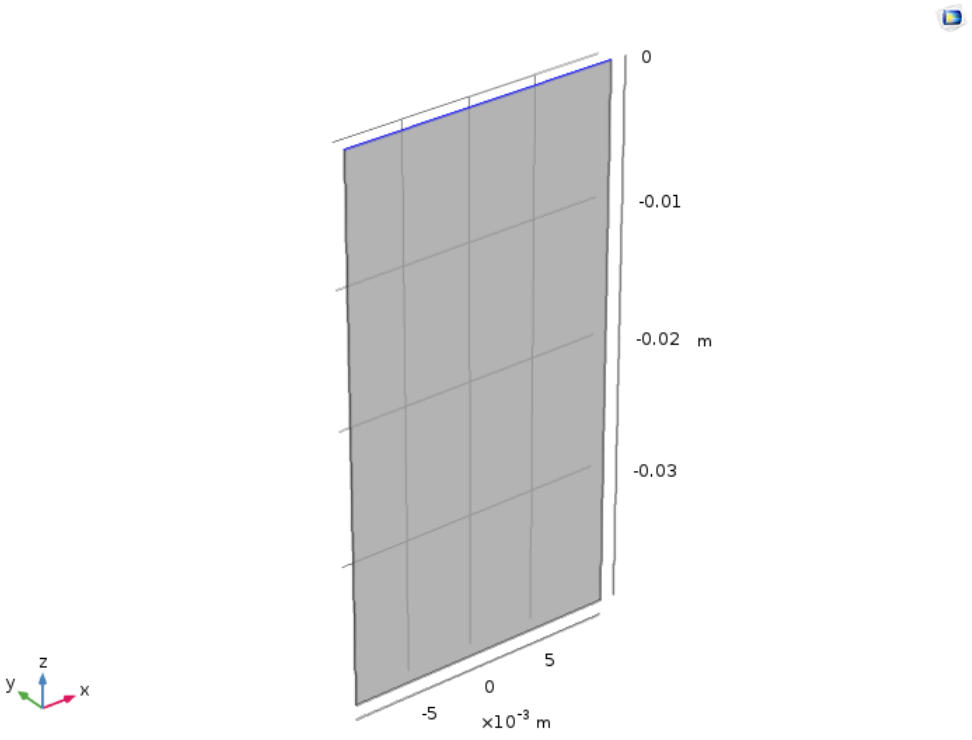

Figure 13: The boundary that is set to experience the predescribed displacement is shown in blue. This whole boundary moves in one of the three Cartesian directions to give birth to the ultrasonic wave.

This predescribed displacement is defined as a 5-cycle Hanning window, which is a cosine function multiplied with a Gaussian to create a finite pulse, as it is shown in Figure 14.

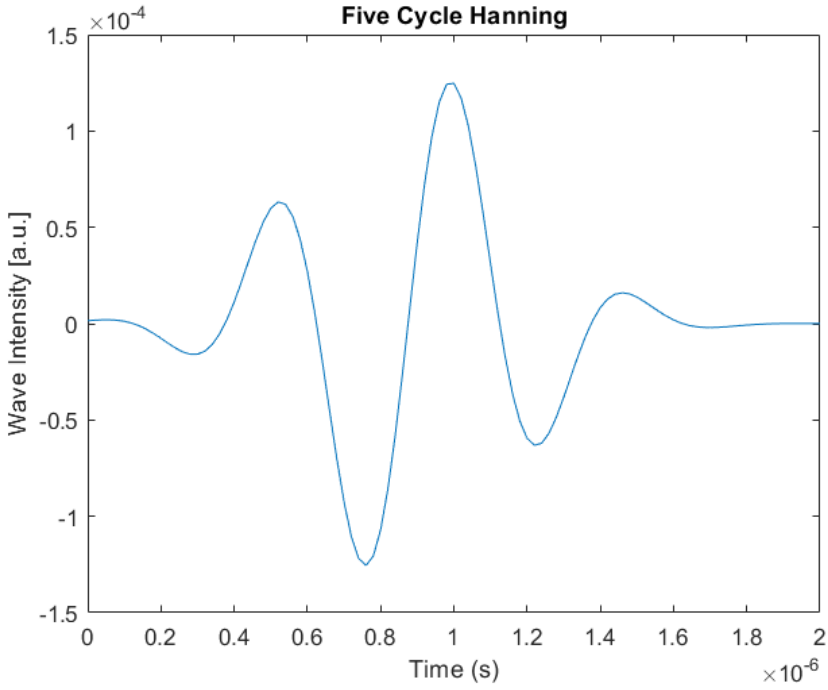

Figure 14: A 5-cycle Hanning window tone burst of $2MHz$.

In the experiment a transducer is used that could send this tone burst at a constant frequency of $3.5MHz$. Desirably the simulations in this research will be done with a $3.5MHz$ pulse, however this is shown to increase the computation time by a factor two [13]. Therefore a frequency of $2MHz$ is chosen for the simulations. The 5-cycle Hanning window shown in Figure 14 is created with the maximum possible time step resulting in the poorest resolution possible. This sample rate equals $50MHz$ which is the minimum Nyquist sampling rate. The minimum time step allowed to be taken by COMSOL Multyphysics is a thousand times smaller, which results in an increase in smoothness of the 5-cycle Hanning window by a factor thousand. The boundaries not experiencing the predescribed displacement are set to be free boundaries. This implies that no forces or constraints are working upon these boundaries.

Voxel size

A convergence study was done, which determined the voxel size [13]. This convergence study has shown that a minimum of eight mesh elements per wavelength is needed for viable results. The relative error in the results was shown to converge to zero with more mesh elements per wavelength. The relative error when using seven mesh elements per wavelength as compared to eight mesh elements per wavelength is smaller than 0.001%. Thus the choice for a maximum voxel size considering eight mesh elements per wavelength is justified. Note that this minimal number of mesh elements is not isotropic as the plate has different dimensions in all three directions. Therefore the voxels used are not cubes but a rectangular cuboids. As the convergence study was not completed for shear waves the assumption is made that at the edges of the waveguide a denser meshsize was needed (see chapter *2.2: Additional wave modes*). This assumption is based on the fact that

shear waves are most interesting at the edges of the waveguide and makes sure that this interesting behaviour is simulated correctly. To tackle this problem an inverse Gaussian distribution of mesh elements is constructed with a minimum number of mesh elements per wavelength (eight) at the centre of the waveguide and a maximum number of mesh elements per wavelength at the edges of the waveguide. This can be seen in Figure 15.

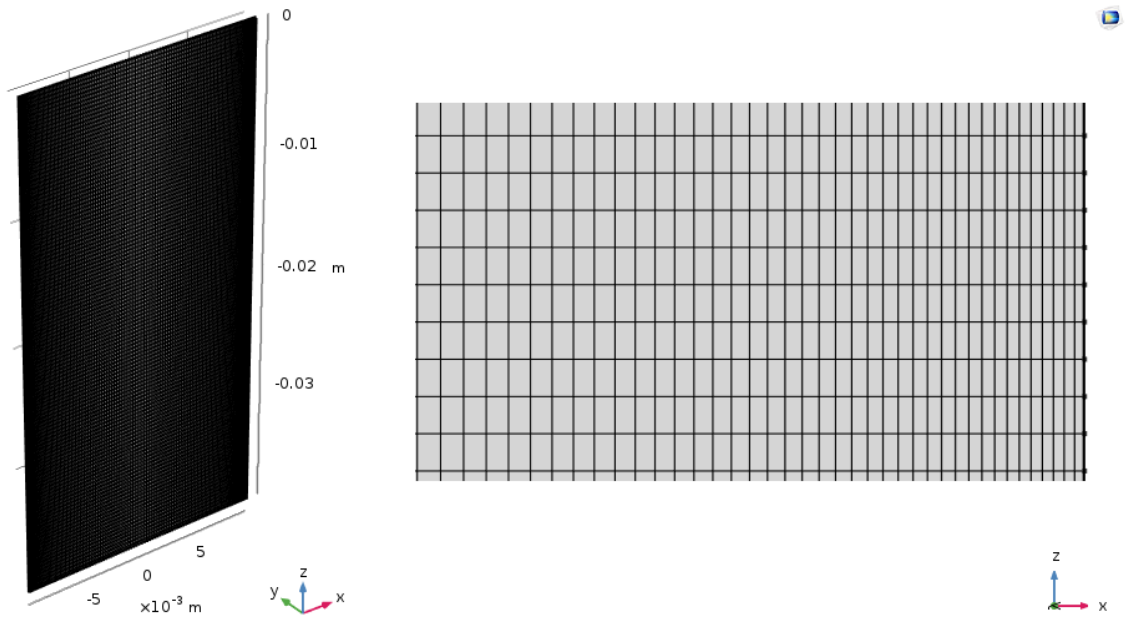

Figure 15: The meshed plate-like waveguide used for the shear wave simulations (left). The inverse Gaussian distribution can be seen in the horizontal (x) direction. At first glace the waveguide seems completely black, this is caused by the dense mesh. On the right a zoomed in section of the right most edge of the waveguide can be seen, where the inverse Gaussian distribution becomes clear.

Simulation and post-processing

The simulations are run on an external server and take about sixty hours on average. These simulation resulted in data files of about one hundred gigabytes. These files need to be downloaded from the server for post-processing. This downloading process usually takes around forty hours. After this process the data files are examined. Two boundary probes are considered: the boundary probe which experiences the predescribed displacement (shown in Figure 13) and a boundary probe at the bottom boundary of the waveguide. At these boundaries different components of the second Piola-Kirchoff stress tensor are examined. For the longitudinal waves the zz component is considered, for the shear waves the xz (or zx) component is considered, and for the flexural waves the yz (or zy) component is to be considered (see chapter *2.3: Continuum Mechanics*). This data is exported from COMSOL Multiphysics and imported into MATLAB. The waves are equipped with their corresponding envelopes and the velocity and attenuation are derived for each wave mode and for each temperature using equations 16 and 17 respectively.

3.2 Experimental set up

The ultimately desired set up is to use the ultrasonic wave technique to measure physical quantities of the molten salt at high temperatures and extreme conditions. To get to that point the prototype set up was made which is shown in Figure 3. The fluid considered is placed in the container and the transducer is placed on top. The experimental set up used to validate the simulation results with empirical data is similar to the prototype set up shown in Figure 3 with the only difference being that the reservoir for possible fluids is removed. This is done because the simulations ran in this research do not include a fluid, but only a plate-like waveguide suspended in air. The physical protoype used can be seen in Figure 16.

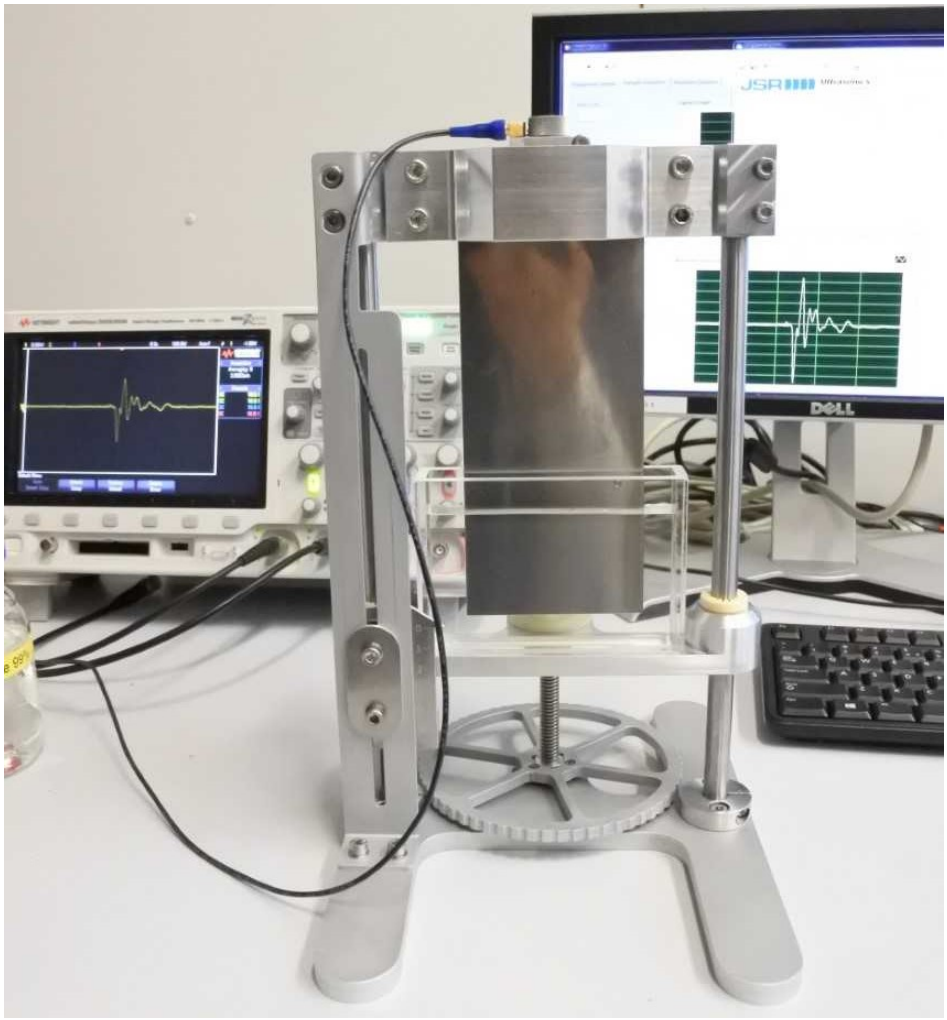

Figure 16: The physical prototype as used in the experiment. In the experiment the fluid container was removed.

Longitudinal ultrasonic wave modes are excited by the transducer at the top, propagate up and down through the waveguide, and are received by the transducer again. The transducer initiates a $3.5MHz$ pulse, as previously mentioned. This excited pulse can be seen in Figure 17.

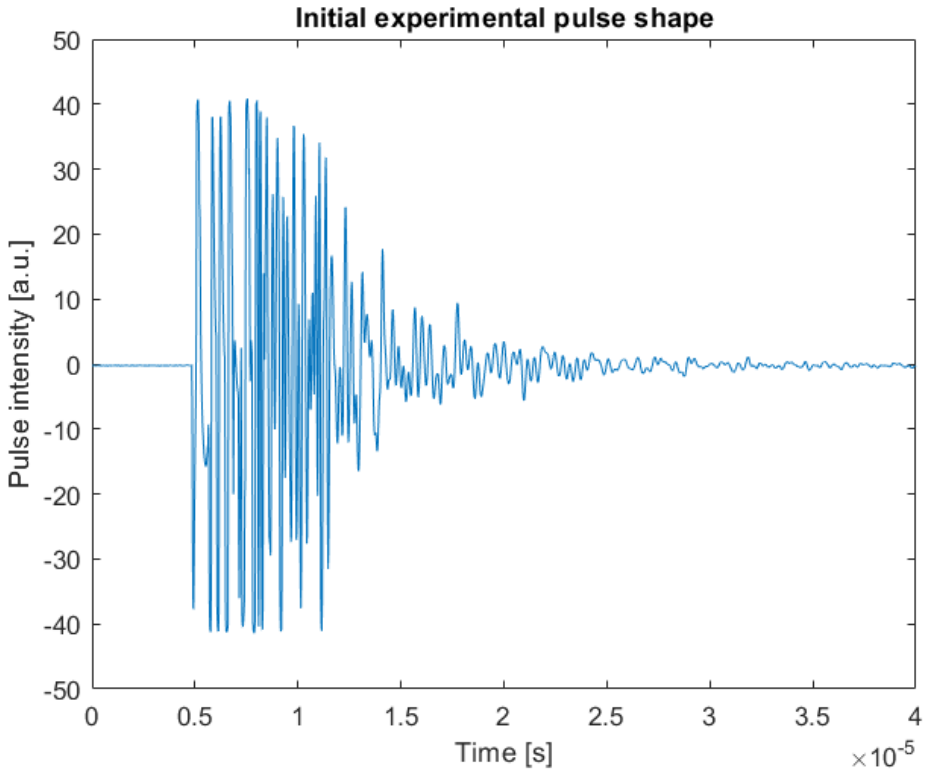

Figure 17: The pulse created by the transducer in the experiment.

The initial created pulse looks as distorted as it is because of the attempt to amplify the pulse as much as possible without making use of an electronic amplifier. The perfomance of piezo-electric transducer peaks, resulting in cut-offs, noisy behaviour, and an aftershock. This amplification is needed because of the high attenuation in the tungsten wave guide, which has dimensions 120 by 80 by 0.2 mm (length $\times$ width $\times$ depth), for longitudinal wave modes. Between the transducer and the waveguide a wave-conducting gel was applied. Interference between the ultrasonic waves and the gel contribute to the noisy signal directly after excitation of the initial pulse as well. The excited pulse could be improved to resemble the pulse shown in Figure 14 with the use of high-end electronic components, which lies outside the scope of this reserach. As this experiment is only used used to couple the results from the simulations to empirical data, the noisy input signal is sufficient. In the experimental case the bottom boundary probe is not considered as a transducer solely exists at the top. The temperature is measured in the experiment both at the bottom and at the top of the waveguide making use of two thermocouples. The transducer is controlled by a LabVIEW script [24] and the response of the transducer is coupled to an oscilloscope. The data from the oscilloscope is exported from LabVIEW and imported into MATLAB for data analysis.

4 Results and discussion

As a first indication the temperature dependent behaviour of the three different moduli (the shear modulus, bulk modulus, and Youngs modulus, covered in chapter *2.3: Continuum mechanics*) was investigated. At first the percentual change of the moduli with the tungsten data from Binkele [20] was plotted. This plot can be seen in Figure 18. This check was done because the three moduli are important indicators of wave behaviour.

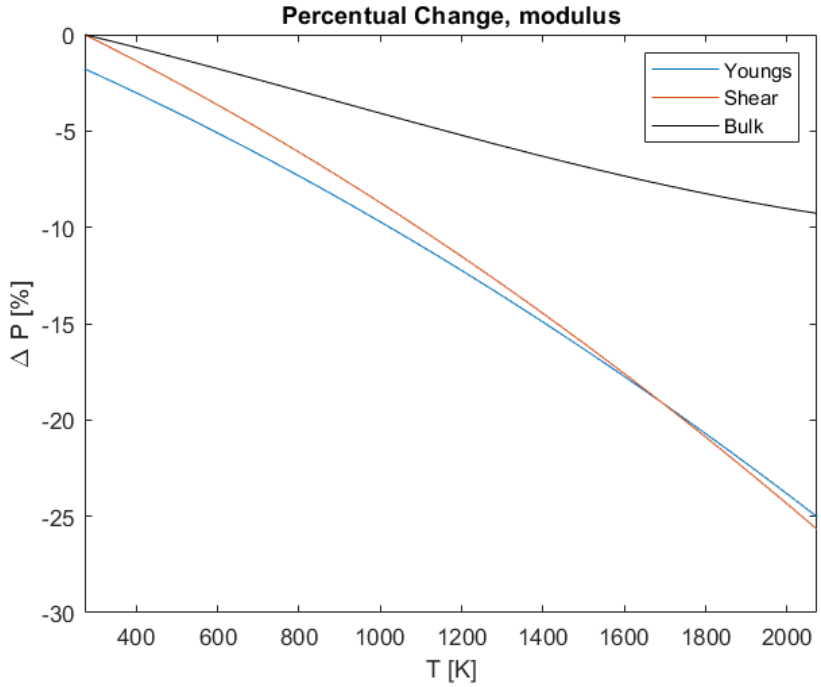

Figure 18: The percentual change of the three moduli (Youngs, shear and bulk) over a temperature range from $300K$ to $2000K$.

From Figure 18 it becomes clear that all three moduli decrease with temperature. The Youngs and shear moduli decrease about 25% over a temperature difference of $2000K$ while the bulk modulus only decreases about 10%. Around the relevant temperatures for an MSFR (around $1000K$, see Figure 2) the Youngs and shear moduli have decreased about 10% from their room temperature value and the bulk modulus about 5%. The reference value of the Youngs modulus is defined in Binkele at $\sim 100K$, which is the reason that the Youngs modulus curve begins at a 2% offset at room temperature. This decrease of the moduli does not imply that, for example, the attenuation should decrease with temperature as well. These moduli appear inversely in the formulae for attenuation (see Equations 9, 10, and 13). To see the effect of the temperature dependent moduli on the attenuation, the same figure as Figure 18 is made, but with the moduli implemented in their respective formulae. For the Youngs and bulk moduli this means that they appear inversely, and one over the square root of the shear modulus is considered. This percentual change can be seen in Figure 19.

From Figure 19 it becomes clear that the attenuation of the waves rather increases instead of decreases with temperature. The biggest increase in attenuation is due to Youngs modulus which rises abound 35%. In the relevant temperature regime the increase of the attenuation

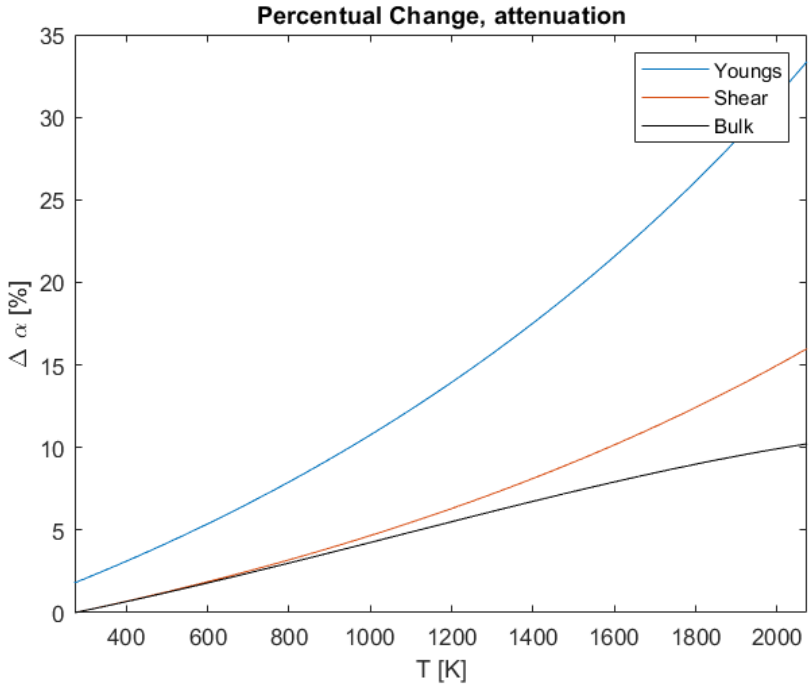

Figure 19: The percentual change of the three moduli (Youngs, shear, and bulk) over a temperature range from $300K$ to $2000K$ implemented in their respective formulae.

due to the shear and bulk moduli accounts for about 5% while the increase of the attenuation due to the Youngs modulus accounts for about 10%.

The shear modulus influences primarily the shear and flexural wave modes while the bulk modulus influences primarily the longitudinal wave modes. However all moduli have an influence on all three primary wave modes as the three moduli completely determine the wave behavior in isotropic materials. The cumulative percentual difference in the attenuation of a wave mode of all three moduli at a temperature of $1000K$ is about $+20\%$ as compared to the attenuation at room temperature. This gives an early indication that temperature dependence in ultrasonic wave attenuation should not be neglected right away.

However, this is just an indication that the temperature dependence of the attenuation of ultrasonic waves cannot be ignored at first glance, and nothing more. The reason for this is that the attenuation is dependent on many more quantities than the three moduli, which may be temperature dependent as well. Think for instance of the density, which decreases with temperature. No qualitative results can be gained from this first analysis. Those qualitative results are expected to be gained from the data analysis of the simulations.

4.1 Longitudinal waves

This section starts with the longitudinal waves, as they are the easiest waves to imagine. The longitudinal waves were excited on the "small" waveguide and were evaluated up until $20\mu s$. The longitudinal waves were able to go back and forth thrice through the waveguide (the longitudinal wave velocity is much higher than the flexural and shear wave velocities [16] [25] (see *Appendix II: Parameters used in COMSOL Multiphysics*)). As already mentioned at

the top and the bottom boundary a probe was placed. The recorded data from both of the probes was equipped with their respective envelopes and the maxima of the wave packages were located for the velocity and attenuation derivations (see chapters *2.5: Wave behaviour and dispersion* and *2.6: Velocity and attenuation calculations*). Seven temperatures were considered in the temperature range from $300K$ ($\sim$ room temperature) up to $1500K$ with steps of $200K$ taken in between (see chapter *3.1: Simulation set up*). The data (the zz component of the second Piola-Kirchoff stress tensor) from both probes (top and bottom) can be seen in Figure 20, evaluated at a temperature of $300K$.

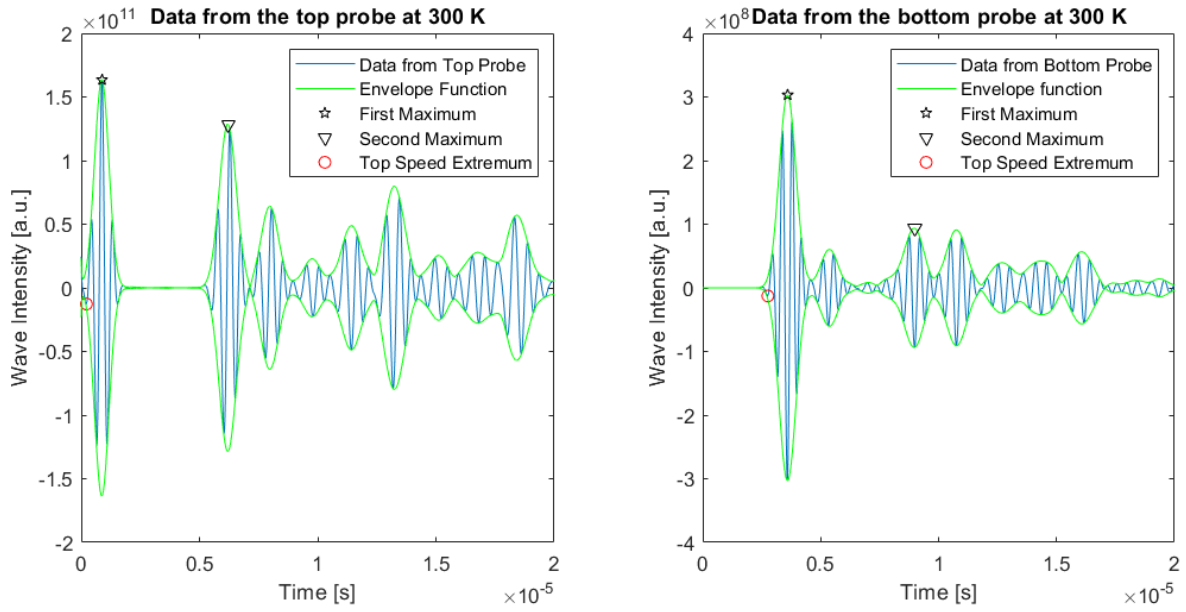

Figure 20: The data from the zz component of the second Piola-Kirchoff stress tensor for the longitudinal waves of both probes at $300K$.

As becomes clear from Figure 20 the longitudinal waves become a lot more dispersed than the flexural and shear wave modes, which will be covered later on. There are no clear pulses arriving at the bottom probe, but rather a continuous stream of different dispersed wave modes. The same holds for the top probe after the first echo has arrived. The top and bottom probe data cannot be combined as the top probe is fixed due to the predescribed displacement (which is a flatline after the 5-cycle Hanning has ended) and the bottom probe behaves as a free boundary, resulting in much higher stress levels ($10^{11}Pa$) measured by the top probe than by the bottom probe ($10^{8}Pa$) (see Figure 20). If the data from the bottom probe is adjusted the two datasets can be superimposed on one another, this is on display in Figure 21. This adjustment means a multiplication of the data from the bottom probe with a large number for the bottom probe data to show stress levels similar to those as measured by the top probe.

From Figure 21 the wave behaviour of the longitudinal waves in the waveguide becomes visible. The longitudinal wave gets excited and makes its way down showing some dispersion. The wave at the bottom probe seems to be completely out of phase with respect to the excited wave as the maxima and minima are reversed. The first echo that arrives at the top probe is a bit more disperse. From the moment that the first echo arrives at the bottom probe on, the influence of the dispersion, trailing echoes, and other additional wave modes, becomes so large that proper data analysis becomes rather difficult. For that reason only

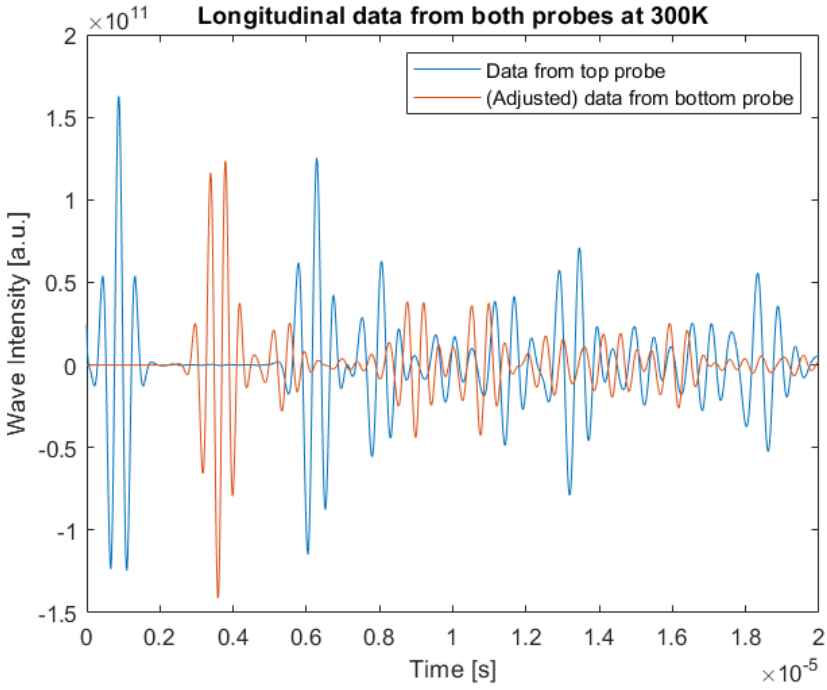

Figure 21: The data from the top and the bottom probe for longitudinal waves at $300K$ superimposed on top of each other. The data from the bottom probe is adjusted by multiplication with a large number to be visible in the graph. The blue curve represents the data from the top probe and the red curve represents the data from the bottom probe.

two points per probe were considered for the velocity and attenuation derivations. These points are given in Figure 20, denoted by the star and the downwards facing triangle. The dispersion and additional wave mode induced problems become even clearer if a surface plot showing the von Mises stress is evaluated at an "early" and "late" point in time, which is shown in Figure 22. In the leftmost Figure displayed in Figure 22 the von Mises stress is imaged at a time of $2.5\mu s$. At this time the ultrasonic wave is on its first way down after excitation. A dispersed wavefront can already be seen alongside with trailing echoes, primarily head waves (see Figure 6), following the initial wavefront closely, just like Froeling already showed [9]. At the later point in time ($17.84\mu s$), shown on the right in Figure 22, it becomes clear that dispersion and the influence of additional wave modes have taken over completely, and it is very hard to tell if the initial wavefront is being considered or some of the trailing echoes. This corresponds to the second half (time-wise) in both graphs displayed in Figure 20, and to the second half (time-wise) of the graph shown in Figure 21. To have an insight in the temperature dependent behaviour of the longitudinal ultrasonic waves the data from one probe, in this case the top probe, is plotted, evaluated at both the lowest and highest temperature considered. This can be seen in Figure 23. From this figure the effect of the temperature on the velocity and attenuation becomes clear immediately. Waves at higher temperature show a lower wave velocity (the echoes arrive at later times at high temperature) and a higher attenuation (the echoes are less intense at high temperature). With the data at the seven different temperatures the determination of the temperature dependence of the velocity and attenuation can be done. This was done for both the data from the top probe and the data from the bottom probe, resulting in two data sets. The

maxima of the wave packets, shown in Figure 20 (star and triangle), are considered and plugged into equation 16. The wave velocity is plotted in Figure 24 from a temperature of $200K$ up until $1600K$. As wave packages are considered for the conclusions, the derived velocity is the group velocity. As the data from the top and the bottom probe should give the same velocities these data sets were averaged to obtain a more qualitative result. The group velocity measured by the top probe is consistently higher than the group velocity measured by the bottom probe. The reason of this lies within the disperse effects of the wave. As the wave shows more dispersion the whole wave package becomes more spread out, shifting the maximum of the wave package to a later point in time, resulting in a lower velocity as measured by the bottom probe (which measures data in a more disperse regime than the top probe).

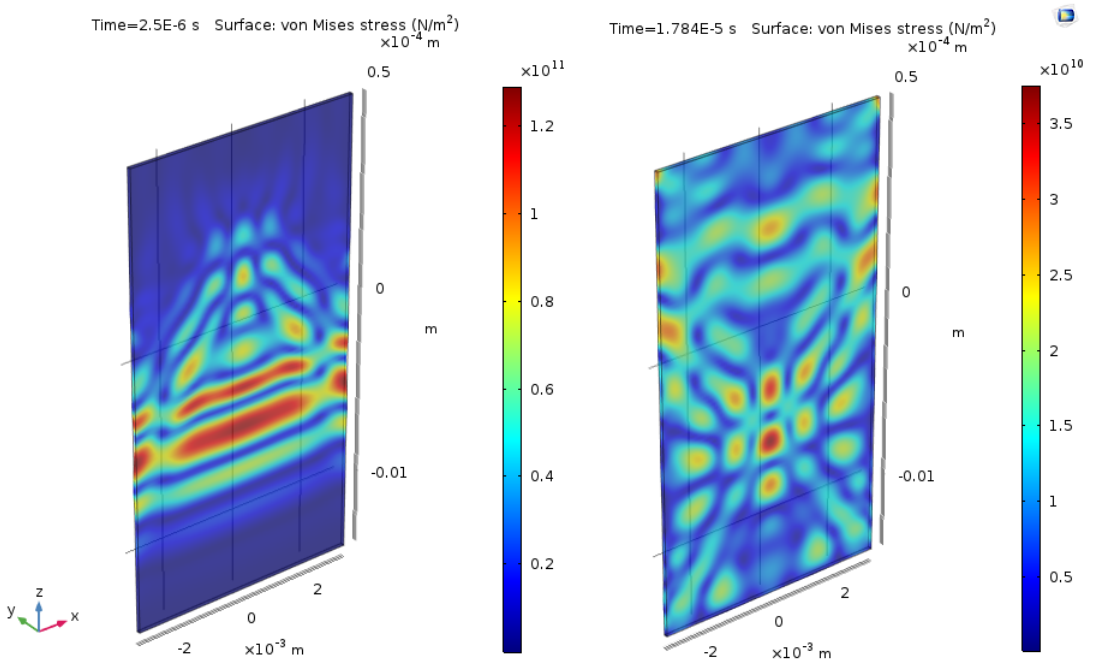

Figure 22: A surface plot showing the von Mises stress for the longitudinal waves at $300K$ at two different points in time: $2.5\mu s$ (left) and $17.84\mu s$ (right).

Since the velocities found are way lower than the literature values found in both Nazarchuck [25] and Rose [16] the "top speed" was looked for in the data. This "top speed" of the wave mode is defined as the very first wave mode that reaches the bottom after excitation. This is derived in the same manner (equation 16), which is applied to the two extrema shown in Figure 20 (denoted by the red circles). This "top speed" is also shown in Figure 24. Though being approximately $250m/s$ higher than the found group velocity the "top speed" still does not agree well with the literature values for longitudinal wave velocity in tungsten of about $5100m/s$. Possible explanations of this deviation will be covered in chapter *4.6: Discussion*. As all of the material properties set by Binkele [20] are defined as simple polynomials it makes sense to fit a simple polynomial (second order in this case) through these data points as well, as shown in Figure 24. The group velocity of the longitudinal wave modes is shown to drop by about $300m/s$ over a temperature difference of $1400K$ semi-linearly. To have a quantitative understanding of this variation, the temperature dependence of the wave velocity is shown in as a percentual change as well, which can be seen in Figure 25.

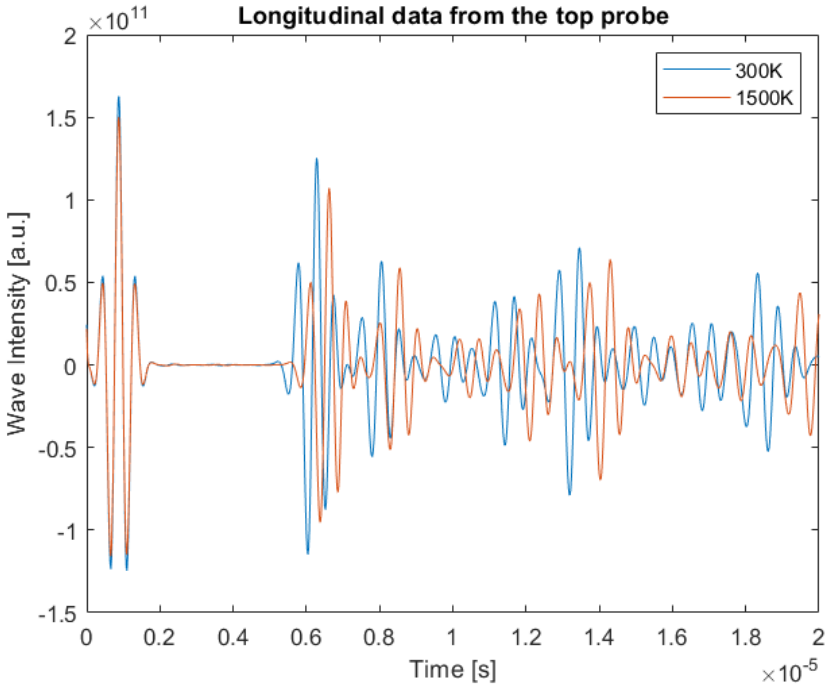

Figure 23: Top probe data from the longitudinal waves evaluated at $300K$ (shown in blue) and at $1500K$ (shown in red).

Through the relative change in velocities another second order polynomial is fitted. Figure 25 shows us that the group velocity and the "top speed" decrease similarly with about a 7% decrease over $1200K$. For the attenuation calculations the same points at the same temperatures were considered as for the velocity calculations, and these points were implemented in Equation 17. The results are shown in Figure 26, and can be found in *Appendix I: Velocity and attenuation results*.

Through these data points a second order polynomial was fitted as well. The attenuation measured by the top probe is considerably lower than the attenuation measured by the bottom probe, due to the dispersion of the longitudinal waves. As already shown in Figures 20, 21, and 22, the longitudinal wave modes become extremely dispersed and influenced by additional wave modes after about $5\mu s$. A higher dispersed wave spreads out the whole wave package, decreasing the intensity considerably. As the considered points for the bottom probe data (Figure 20) exist within this disperse domain (especially the second considered maximum) the attenuation found for the bottom probe differs by a factor four. Regardless of the different attenuation values the same temperature dependent behaviour is found, showing a semi-linear curve upwards. An increase in temperature of $1400K$ gives rise to an increase in the attenuation of about $4Np/m$. It is insightful to consider the behaviour of the attenuation relatively as well, which is shown in Figure 27.

The relative data shows an increase in the attenuation with temperature. In the non-disperse regime longitudinal wave attenuation rises with about 40% over a temperature difference $1400K$. However when the wave has become heavily dispersed the attenuation only shows an increase of about 7% over the same temperature range. This indicates that when a wave has become dispersed the attenuation is less affected by the temperature, however the attenuation of non-dispersed longitudinal waves is influenced heavily by temperature.

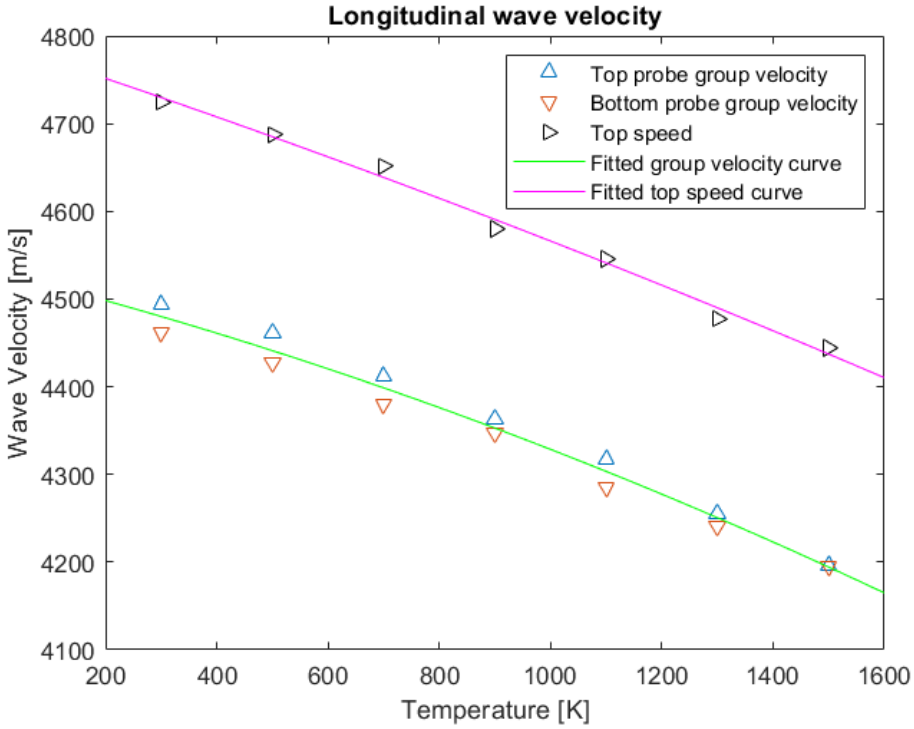

Figure 24: The temperature dependency of the ultrasonic wave velocity for longitudinal wave modes. The data from the top and from the bottom probe are shown as the upward (blue) and downward (red) facing triangles respectively. The "top speed" data is shown as the black triangle.

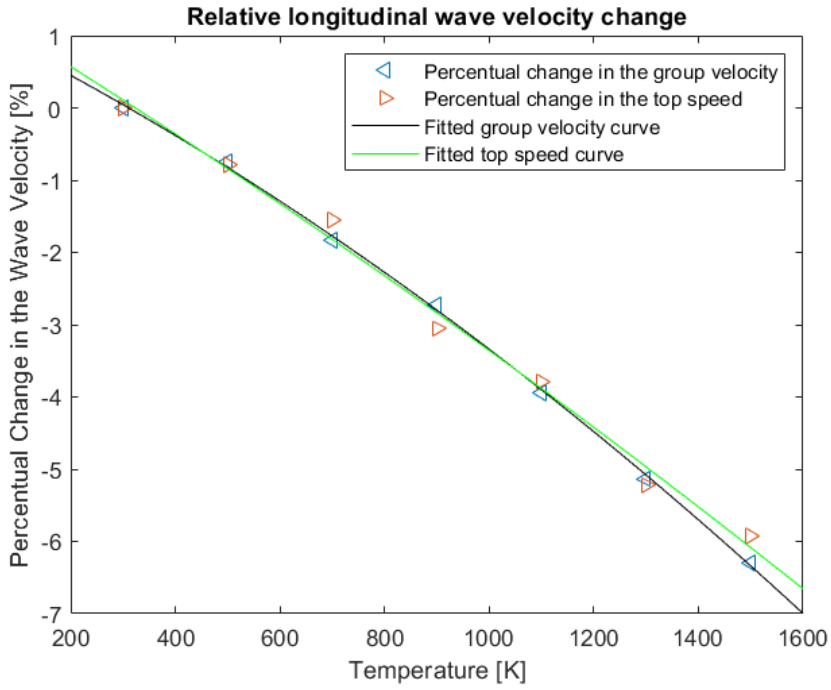

Figure 25: The relative change in the group velocity and the top speed of the longitudinal ultrasonic wave modes.

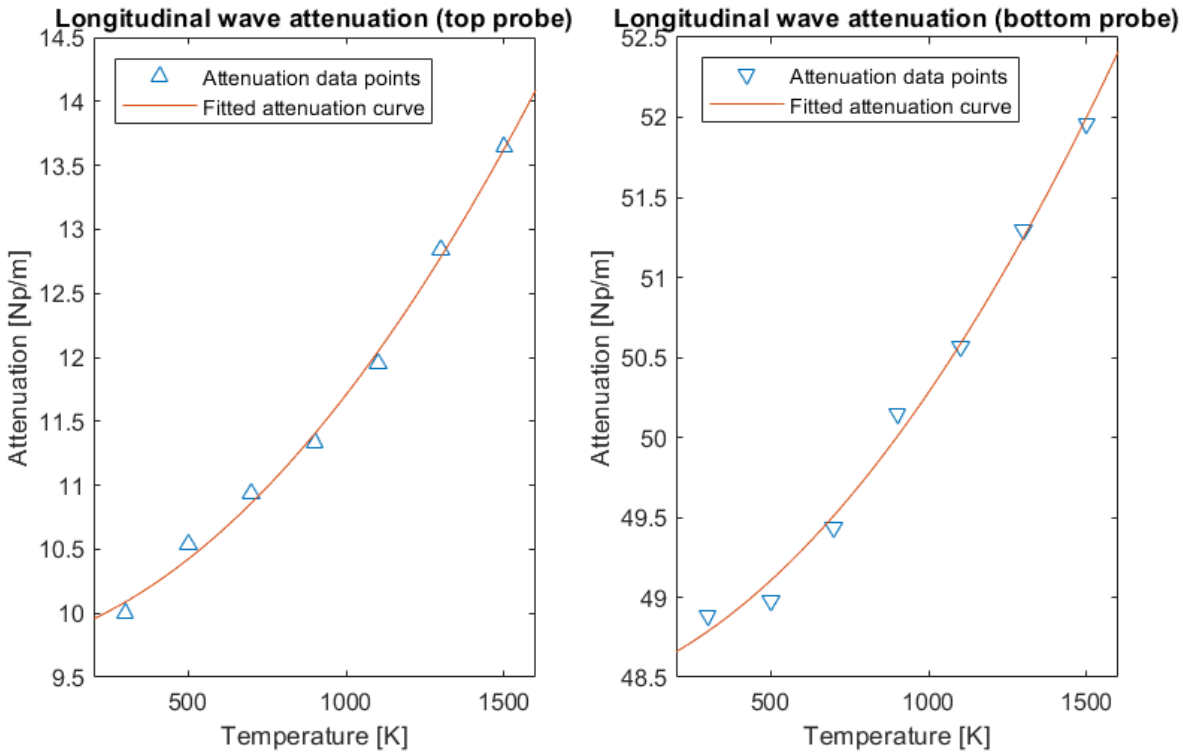

Figure 26: The temperature dependent behaviour of the attenuation of longitudinal wave modes, evaluated at the top probe (left) and at the bottom probe (right).

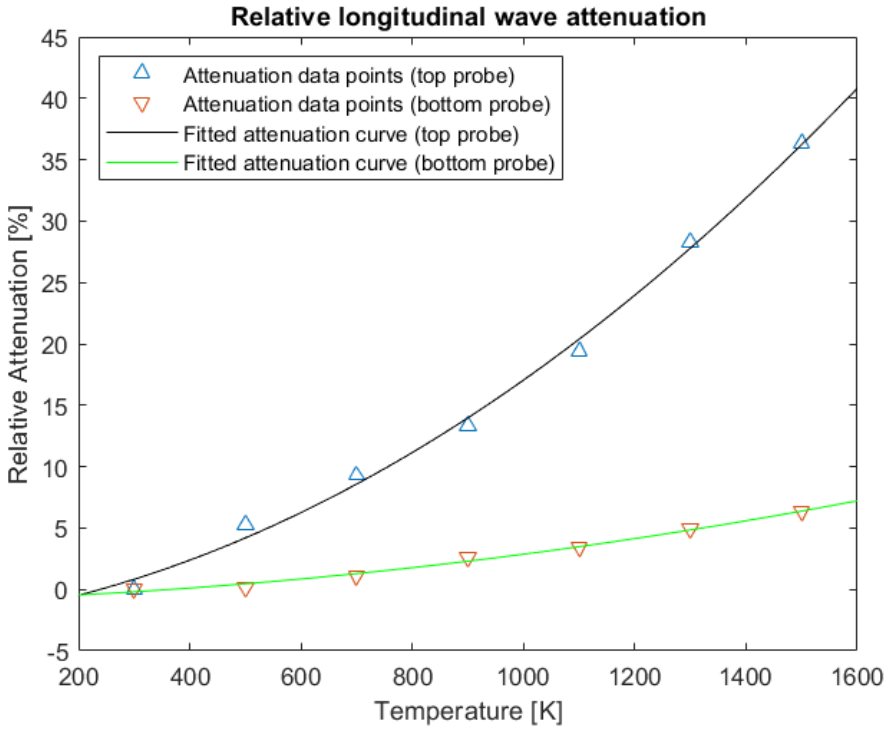

Figure 27: The relative temperature dependence of the attenuation as recorded by both the top curve (yellow) and the bottom curve (purple) for longitudinal waves.

From the results of the longitudinal wave modes it can be concluded that the use of longitudinal wave modes is discouraged for the molten salt measurements. It has again been shown that longitudinal waves in plate-like waveguides are heavily disperse and problematically influenced by additional wave modes. The attenuation of disperse waves is shown to vary little with temperature, which is beneficial for the molten salt experiments, but with such disperse wave modes, and the additional wave modes, the identification of correct wave modes becomes troublesome, especially when in the molten salt experiments new additional wave modes, like the quasi-Scholte mode, come into play as well. The longitudinal wave velocity is shown to drop with 7% over $1400K$ while the attenuation of non-disperse waves rises with 40% over the same temperature range. As stated before, all of the data points can be found in *Appendix I: Velocity and attenuation results*.

4.2 Flexural waves

Secondly the flexural waves will be considered. The flexural waves were excited on the "small" waveguide and were evaluated up until $30\mu s$. In this time period the flexural waves were able to traverse up and down the waveguide two and a half times, illustrating the lower flexural wave velocity as compared to the longitudinal wave velocity. At the top and the bottom boundary probes were created. The recorded waves from both probes were plotted with their respective envelope functions and the maxima were identified. Similar to the longitudinal waves seven different temperatures were considered: $300K$ to $1500K$ in steps of $200K$. The data from both probes (the yz component of the second Piola-Kirchoff stress tensor), evaluated at $300K$, can be seen in Figure 28.

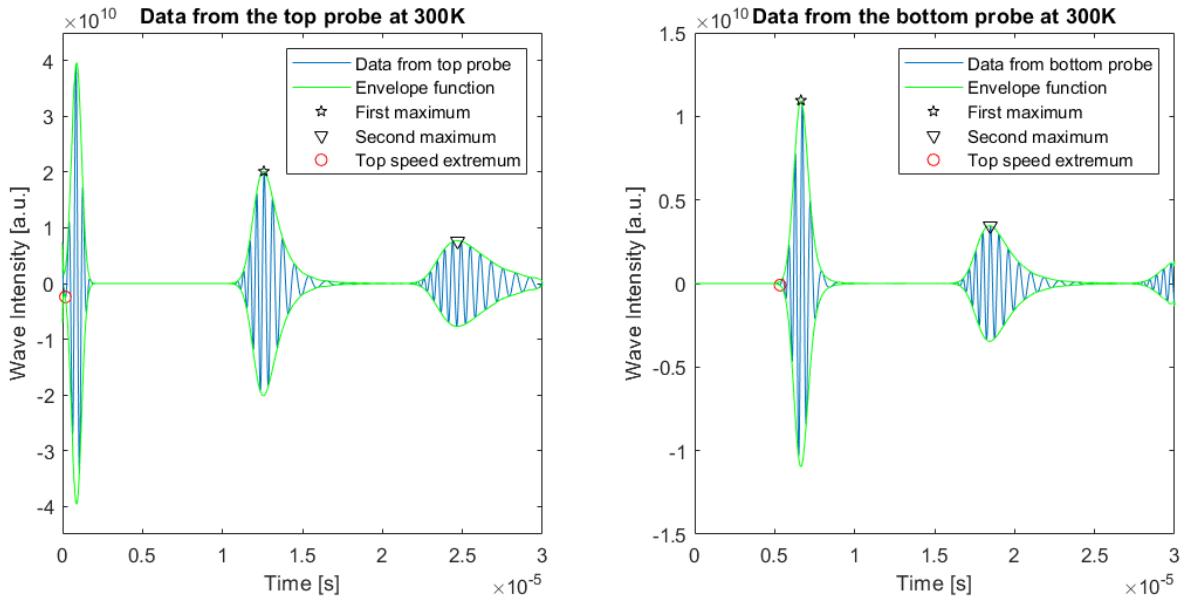

Figure 28: The data of the yz component of the second Piola-Kirchoff stress tensor for the flexural wave modes, considered at both probes at a temperature of $300K$.

From Figure 28 it becomes clear that flexural waves disperse less than longitudinal waves. At both probes three clear distinguishable peaks can be seen (although the last echo at the bottom probe is cut off). Again the data can not be visualized in one graph because of

the top probe being stiff after the predescribed displacement and the bottom probe being a free boundary. The data from the bottom probe can be adjusted and the "footprint" of the wave can be seen, this is displayed in Figure 29.

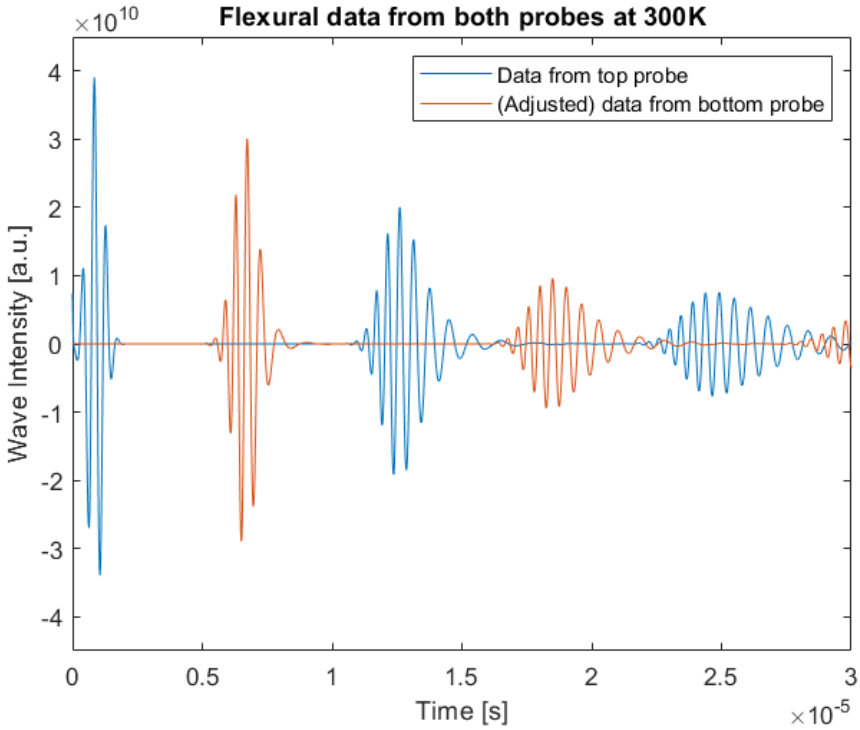

Figure 29: The superimposed data sets from the flexural waves. Neat behaviour of the wave can be seen traversing up and down along the waveguide.

The wave can be seen becoming more and more dispersed with every arrival at one of the probes (every recorded wave package is more spread out than the one before) but the influence of additional wave modes and trailing echoes is minimal. Because of the cleanness of the signal, for the top probe the maxima of the two echoes were considered for the calculations of the velocity and attenuation, which can be seen in Figure 28. This holds two advantages over choosing the first peak. The first one of which is that the first peak is always the same height (or intensity) as it is defined by the predescribed displacement, and therefore holds no information about the wave behaviour inside the waveguide. The second reason is that the second and third maxima are located in the more disperse regime of the wave modes, just like the data from the bottom probe. In this way two data sets are created which describe the behaviour of the wave in approximately the same dispersion-environment, which enables certain comparisons between the two (top and bottom probe) derived attenuations. This is only done for the flexural waves, and not for the longitudinal and shear (which will be covered later on) because it was not possible for the other wave modes. The longitudinal wave modes showed too much dispersion and interference from additional wave modes to correctly identify the second echo at the top probe. For the shear waves the time range considered was to short to measure the arrival of the second echo at the top probe. From the bottom probe the only two maxima fully displayed within Figure 28 were considered. The lack of dispersion shown by the flexural waves is depicted in two surface plots of the von Mises stress at two different points in time, displayed in Figure 30.

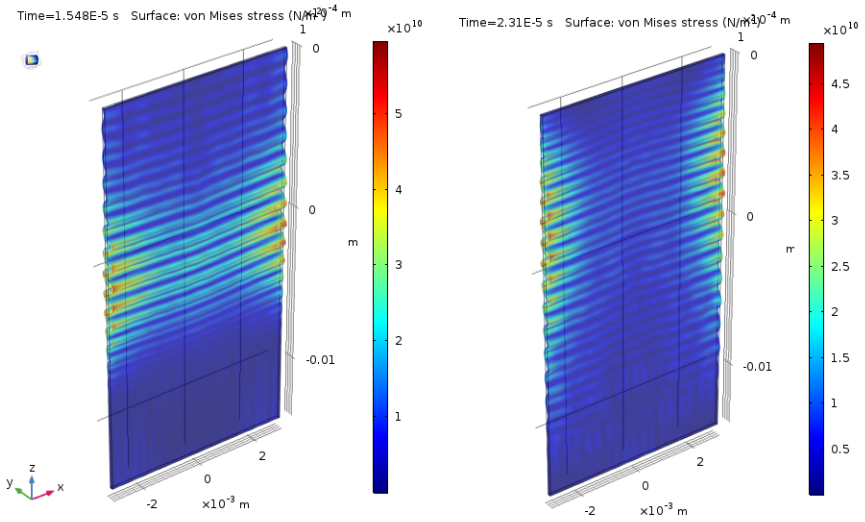

Figure 30: Two surface plots showing the von Mises stress of the flexural waves at two points in time at a temperature of $300K$: $15.48\mu s$ on the left and $23.1\mu s$ on the right. The deformation is shown in an exaggerated manner.

From this figure it becomes clear that the trailing echoes are non-existent and that the flexural waves attenuate the most in the center of the waveguide, while attenuating less at the edges. To have a first indication of the effect of temperature on the attenuation and wave velocity of the flexural wave modes, the data from the lowest and highest temperature are shown in the same figure (Figure 31).

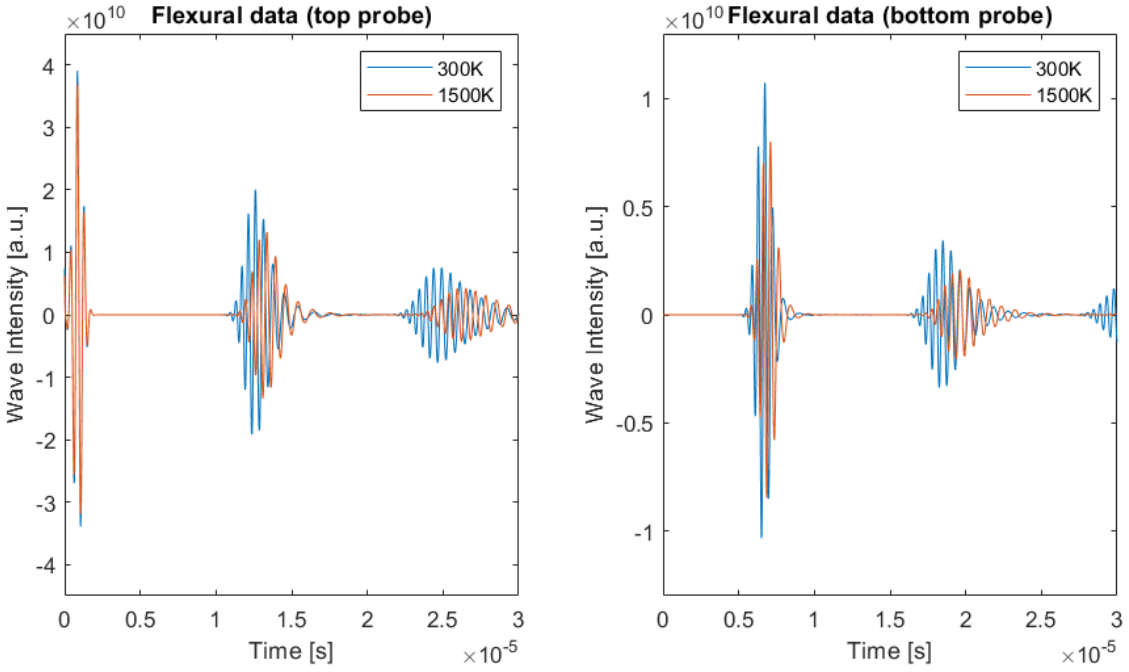

Figure 31: The yz component of the second Piola-Kirchoff stress tensor at the lowest (blue) and highest (red) temperature in the same graph for the flexural waves as measured by the top probe (left) and the bottom probe (right).

This graph immediately shows the lower wave velocity and higher attenuation at higher temperatures, similar to the longitudinal waves. The maxima denoted by the star and the downward facing triangle (Figure 28) are considered for the attenuation and velocity calculations. Again the top and bottom probe data considering the velocities was averaged as they should give the same result. The obtained velocities and their temperature dependence is shown in Figure 32. Again the velocity measured by the top probe is higher than the velocity measured by the bottom probe due to disperse effects. All of the used data points can be found in *Appendix I: Velocity and attenuation results*.

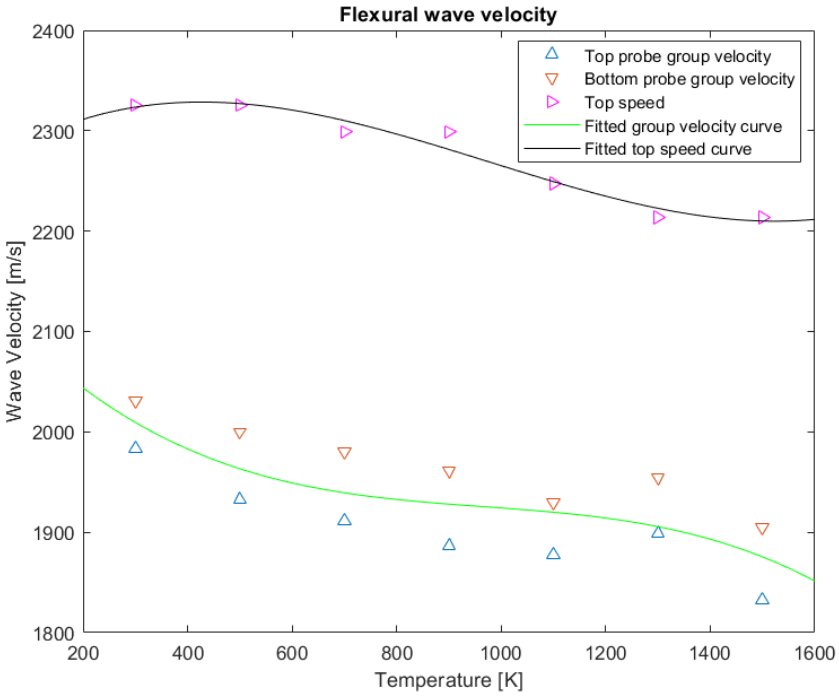

Figure 32: The temperature dependency of the ultrasonic wave velocity for flexural wave modes. The data from the top and bottom probe is shown as the upward (blue) and downward (red) facing triangles respectively. The "top speed" data is shown as the purple triangles.

The velocities for the flexural waves were again found to be much lower (by about $500m/s$) than the literature values found in Rose [16] and Nazarchuck [25]. This velocity is the group velocity of the flexural waves as they show dispersion, though not as much as the longitudinal waves, and thus this group velocity (the velocity of the wave packages) is not equal to the phase velocity. Due to the deviation from the literature values the "top speed" was sought and found as well (also shown in Figure 32), which still turned out be much lower than the literature value for flexural wave velocities. This will be discussed later on in chapter *4.6: Discussion*. Simple polynomials were fitted through the data points to follow the approach of Binkele [20]. The group velocity of the flexural waves drops quasi-linearly with $150m/s$ over a temperature increase of $1400K$, which is a 50% less decrease as compared with the longitudinal velocity drop over the same temperature range. A found difference is that around $1300K$ the group velocity seems to go up rather than down, after which it drops again, which was not found with the longitudinal waves. This "bump" will be discussed later on. The relative change in velocity is shown in Figure 33.

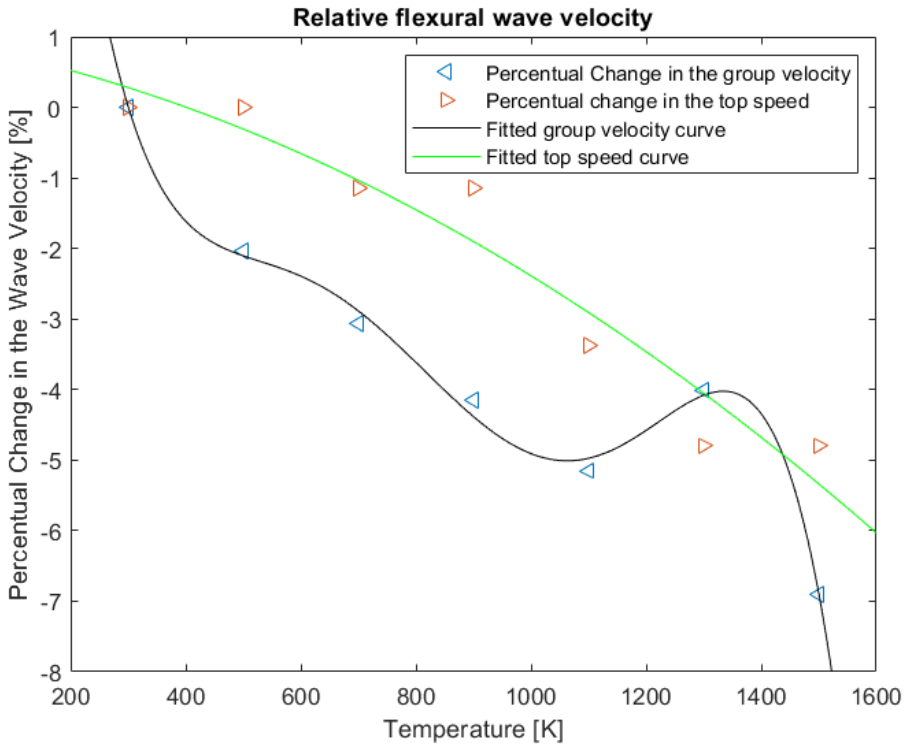

Figure 33: The relative change in both the group velocity and the "top speed" for the flexural wave modes.

The "top speed" show the same semi-linear relative behaviour as both the group velocity and the "top speed" from the longitudinal wave modes. However, partially due to the "bump" at $1300K$ in the group velocity, the relative curve of the group velocity has lost its linear component. It shows a semi-linear decrease between $400K$ and $1000K$, whereafter it "bumps up" and "shoots down". Similar findings have been shown by Papadikis [19]. The given cause for this was the transition of the crystal structure of the considered metal from body centered cubic to face centered cubic. In the operational regime of molten salt reactors (up until $1100K$) the curve can be approximated to be linear, showing a 4% decrease over an increase in temperature of $800K$, similar to the longitudinal wave modes.

For the derivation of the attenuation the same data points are considered as for the velocities (star and triangle in Figure 28) and were implemented in Equation 17. These results are shown in Figure 34.

A higher order polynomial was fitted through the data to ease the interpretation of the temperature dependency of the attenuation, but no qualitative results should be obtained from this polynomial. More data points are needed for qualitative information of the attenuation of flexural waves in this temperature range. The attenuation as measured by the top probe only differs by $5Np/m$ from the attenuation as measured by the bottom probe. The reason for this is that the data from both probes consists of waves showing (approximately) equal dispersion. The data from both probes shows a curve which is parabolic in the region between $500K$ and $1100K$, then suddenly drops, and rises again. Similar attenuation behaviour is found by Papadikis [19] and Basu [26] for longitudinal waves, but not for flexural waves. This remarkable difference will be discussed later on in chapter *4.5: Comparison*

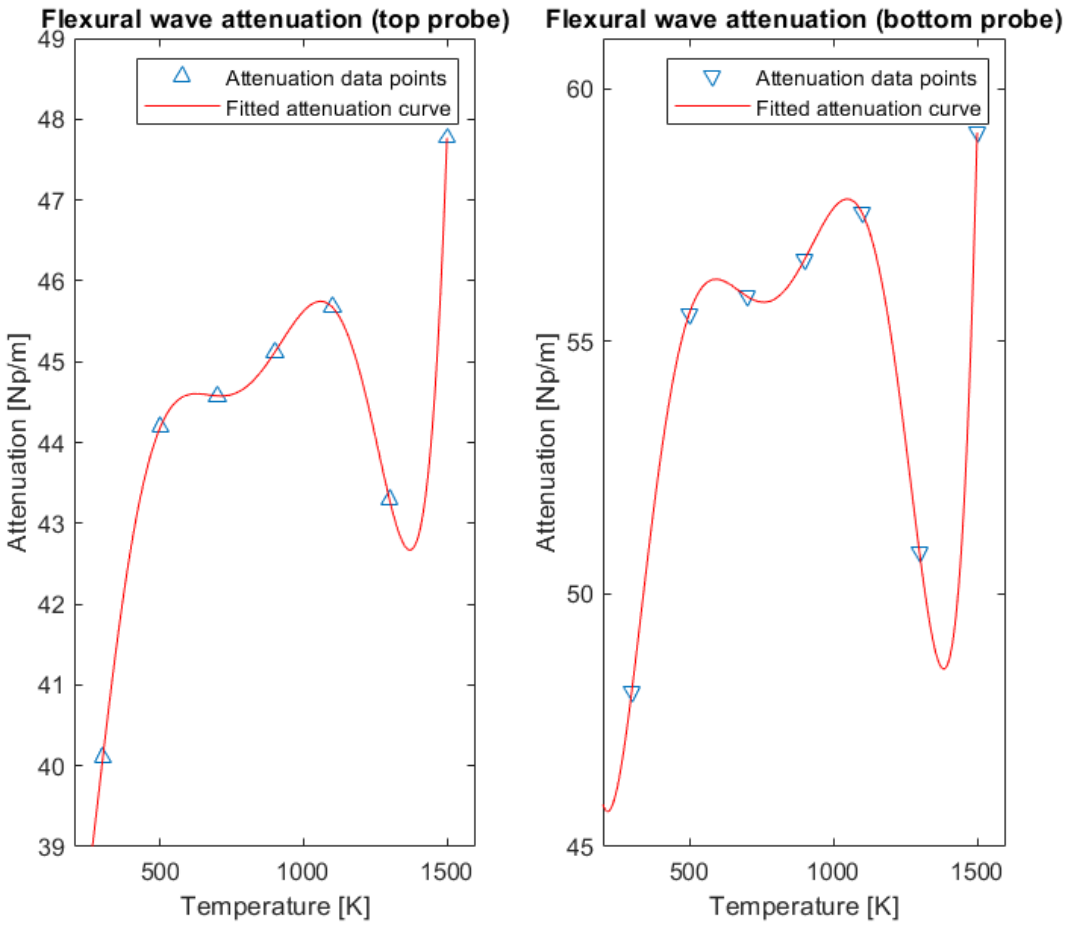

Figure 34: The temperature dependence of the attenuation as observed by the top probe (left) and the bottom probe (right) for the flexural wave modes.

with literature. The values of the attenuation (between $40Np/m$ and $60Np/m$) are in good agreement with the data from Papadikis for their respective temperatures. Over the whole considered temperature spectrum ($300K$ to $1500K$) the attenuation increased by about $10Np/m$. The increase from room temperature ($\sim 300K$) to operational temperatures of an MSFR ($\sim 1000K$) gives birth to an increase in the attenuation of only $6Np/m$. The "unusual" dip in the attenuation for both probes occurs at the same temperature ($1300K$) as the "unusual" bump in group velocity, shown in Figure 32 and Figure 33. This suggests that more research on the temperature dependency of the attenuation and velocity needs to be done using $2MHz$ pulses though a tungsten waveguide in that particular vicinity. The behaviour of the attenuation is also shown relatively in Figure 35.

The figure displaying the relative behaviour of the attenuation (with similar polynomials as used in the absolute attenuation graph) shows the same shape as the curves in Figure 34. Over the whole temperature range the attenuation is shown to increase by 20%, which again is 50% less than the attenuation increase of the longitudinal waves over the same temperature range. This indicates that the temperature dependent properties of the attenuation of flexural waves is twice as weak as those of longitudinal waves. Increasing the temperature from room temperature to MSFR operational temperatures gives rise to an $\sim 12\%$ increase in the attenuation.

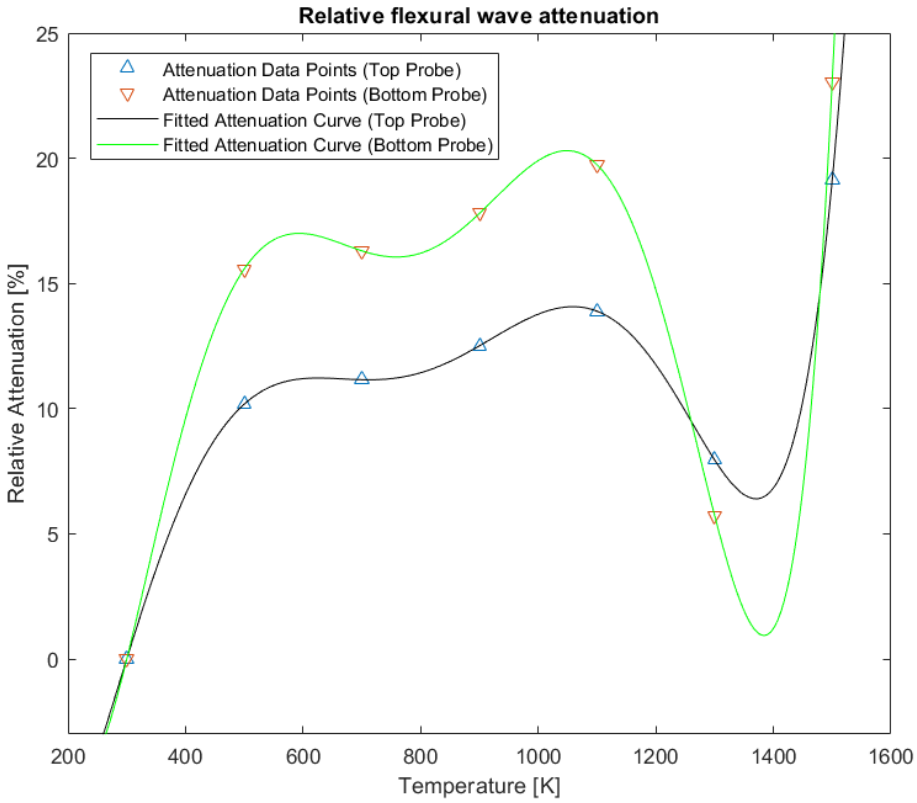

Figure 35: The relative temperature dependence of the attenuation as observed by the top probe (black) and the bottom probe (green) of the flexural wave modes.

From the results of the flexural wave modes it can be concluded that the flexural wave modes are a much better fit than the longitudinal wave modes for the intended molten salt measurements as they are less disperse and not influenced by additional wave modes at all. However (especially) the attenuation shows less predictable behaviour over temperature than the attenuation of the longitudinal waves. Unusual behaviour is shown around a temperature of $1300K$ for both the group velocity and the attenuation, which needs to be investigated further if a complete understanding of this temperature dependence is desired. The group velocity was shown to drop with 4% over $800K$ and the attenuation increases about $12Np/m$ over $700K$. Temperature dependencies on the attenuation seemed twice as weak as compared to the longitudinal waves. As stated before, All of the data points used can be found in *Appendix I: Velocity and attenuation results*.

4.3 Shear waves

Thirdly the shear waves were evaluated. The shear waves were excited on the "big" waveguide to ensure that an appropriate value for the frequency wideness is acquired (see chapter *2.2: Additional wave modes* and *3.1: Simulation set up*). The shear waves were evaluated up until $50\mu s$ in which the shear waves were able to traverse up and down the waveguide twice. Probes were created at the upper and lower boundary of the waveguide. Envelope functions were calculated and put on top of the recorded data, from which the maxima of

the main wave packages were found. Again the same temperature range ($300K$ to $1500K$ in steps of $200K$) was considered. The data from both probes (the xz component of the second Piola-Kirchoff stress tensor), at $300K$, can be seen in Figure 36.

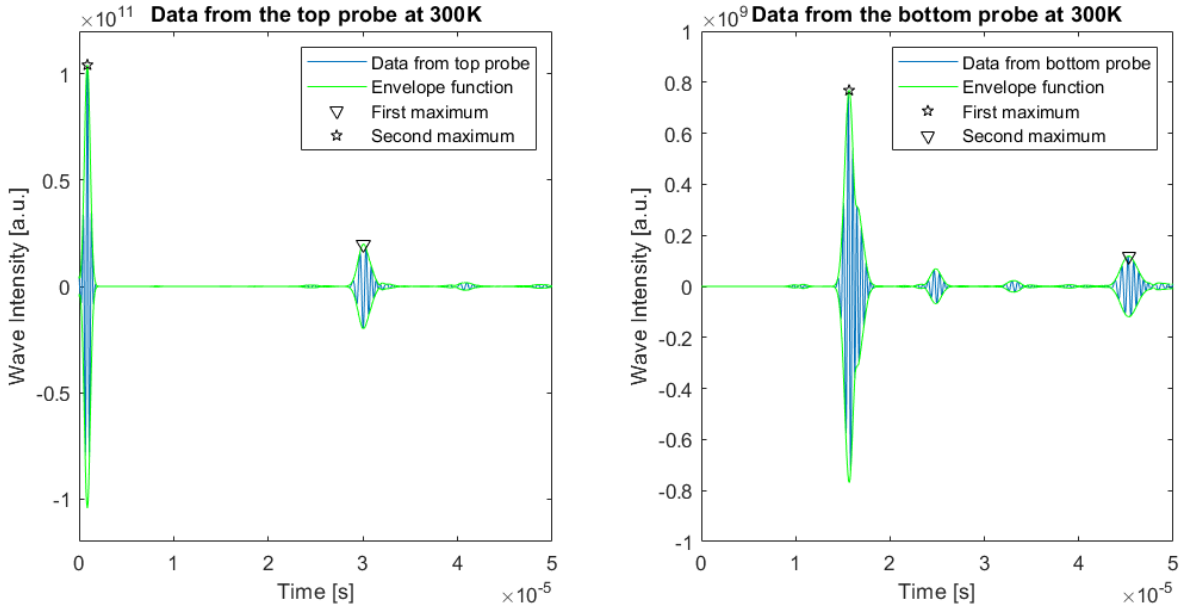

Figure 36: The data (xz component of the second Piola-Kirchoff stress tensor for the shear waves evaluated at the top probe (left) and the bottom probe (right) at $300K$.

These shear waves are way less disperse than the longitudinal and the flexural waves. However the shear waves are more prone to additional wave modes and trailing echoes than the flexural waves are. For example at the bottom probe clearly an additional wavemode is recorded around 25 μs. The dispersion and influence of additional wave modes on the shear waves is acceptable as all peaks remain isolated and are clearly distinguishable from one another. Therefore this disperse behaviour is not problematic. Again the data can not be visualized in one graph as the stress levels at the boundary executing the predescribed displacement (top) is three orders of magnitude bigger than the stress levels at the free boundary (bottom). If the data from the bottom probe is adjusted the "footprint" of the wave behaviour becomes clear again, which is seen in Figure 37.

The wave packages can be seen getting more dispersed and attenuated over time and the presence of one clear trailing echo is seen (appearing first around $25\mu s$). The peaks of the first and second recording of the primary shear wave mode for both probes was chosen for the velocity and attenuation calculation (denoted in Figure 36). A surface plot showing the von Mises stress is made to display the creation of the trailing echo and the ultimately disperse behaviour and influence of additional wave modes of the shear waves at the latest point in time considered ($50\mu s$). This is shown in Figure 38.

In the leftmost surface plot the trailing echo can (vaguely) be seen tailgating the primary wave mode. It can also be seen that the primary shear wave mode in the middle of the waveguide is not in phase with the same wave mode at the edges of the waveguide, which was already predicted by Cegla [7]. In the rightmost surface plot the dispersion and additional wave modes can be seen at a later point in time. Although disperse behaviour and the influence of additional wave modes have taken over the whole waveguide, the primary wave

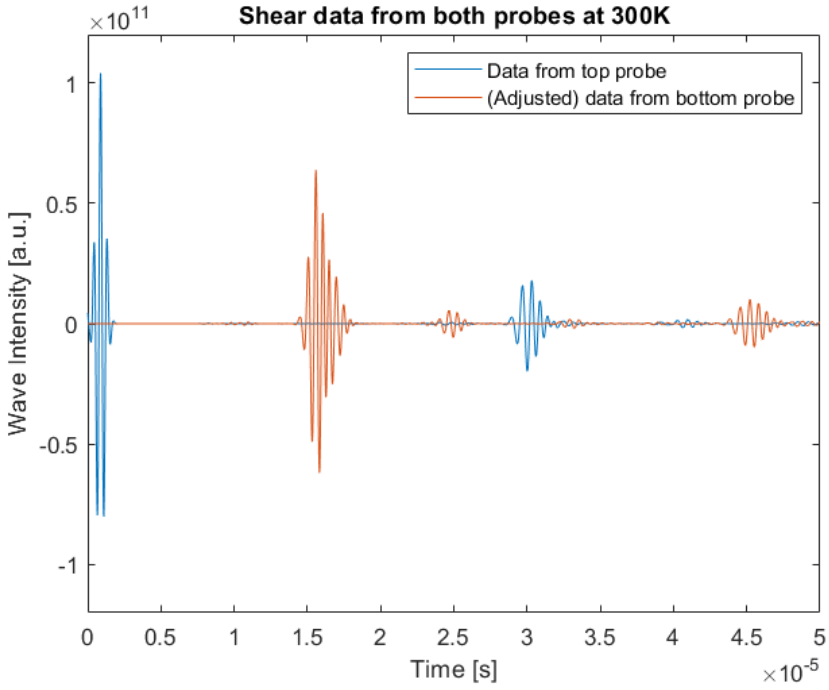

Figure 37: The superimposed data of the shear waves from both probes: top (blue) and bottom (red), at $300K$.

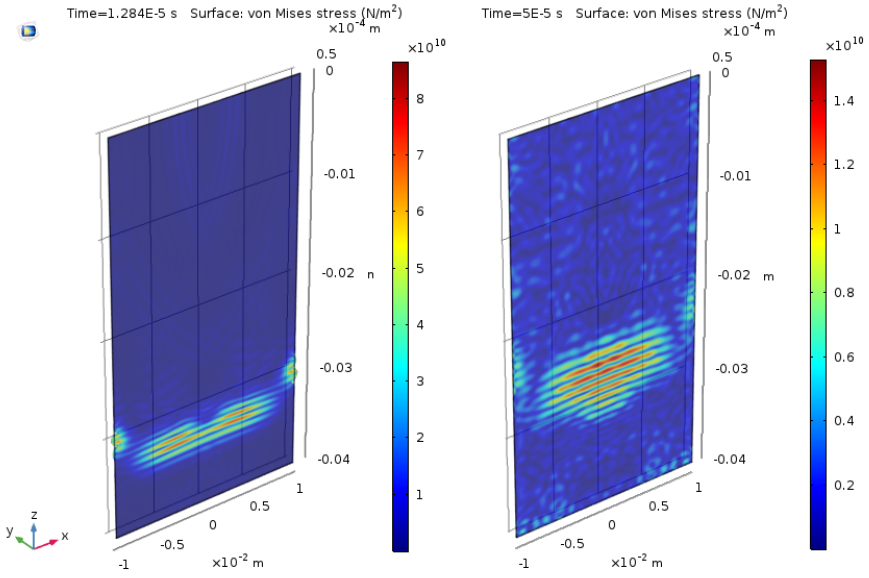

Figure 38: A surface plot showing the von Mises stress along the waveguide for the shear waves at $300K$ at two different points in time: $12.84\mu s$ (left) and $50\mu s$ (right).

mode is still clearly distinguishable, which is also seen in the probe plots (Figure 36). To have an indication of the temperature dependent behaviour of the attenuation and velocity of the shear waves the data from the top probe at the lowest and highest temperature considered ($300K$ and $1500K$) was displayed inside the same figure (Figure 39).

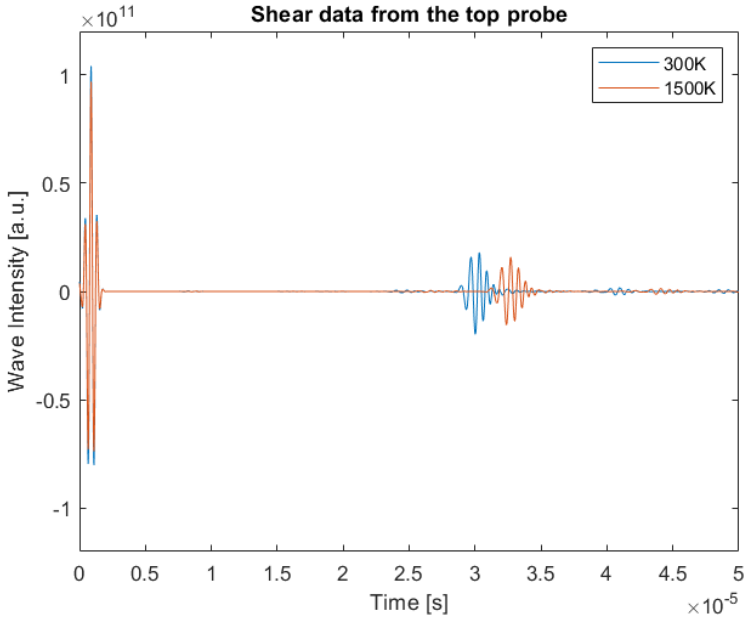

Figure 39: The recorded data (the xz component of the second Piola-Kirchoff stress tensor) from the top probe at $300K$ (blue) and $1500K$ (red).

The lower group velocity at the high temperature becomes apperent right away and also slight attenuational differences can be seen between the two temperatures. First the velocities were investigated with the maxima from Figure 36 and equation 16. The velocities of the top and bottom probe were averaged into one simple polynomial for a more qualitative result. This can be seen in Figure 40. Once more all of the velocities found by the top probe are higher than the velocities found by the bottom probe due to dispersion. All of the used data points can be found in *Appendix I: Velocity and attenuation results*.

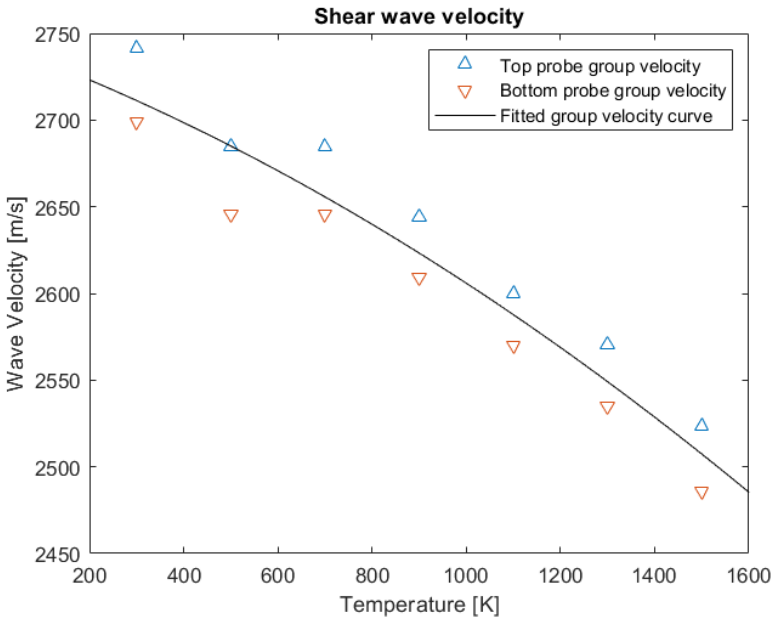

Figure 40: The temperature dependent behaviour of the group velocity for shear waves.

These velocities found are in much better agreement than the literature values found in Nazarchuck [25] and Rose [16] ($\sim 3\%$ deviation) than the longitudinal and shear wave modes. These velocities found need to be considered as the group velocities as they display the velocity of wave packages as a whole. This velocity is not equal to the phase velocity as disperse effects arise over time. A simple polynomial is used, again following the approach of Binkele [20]. An $200m/s$ drop is found over a temperature increase of $1300K$. To get a better understanding of how influencing this decrease in velocity is, the relative change in velocity is plotted as well (Figure 41).

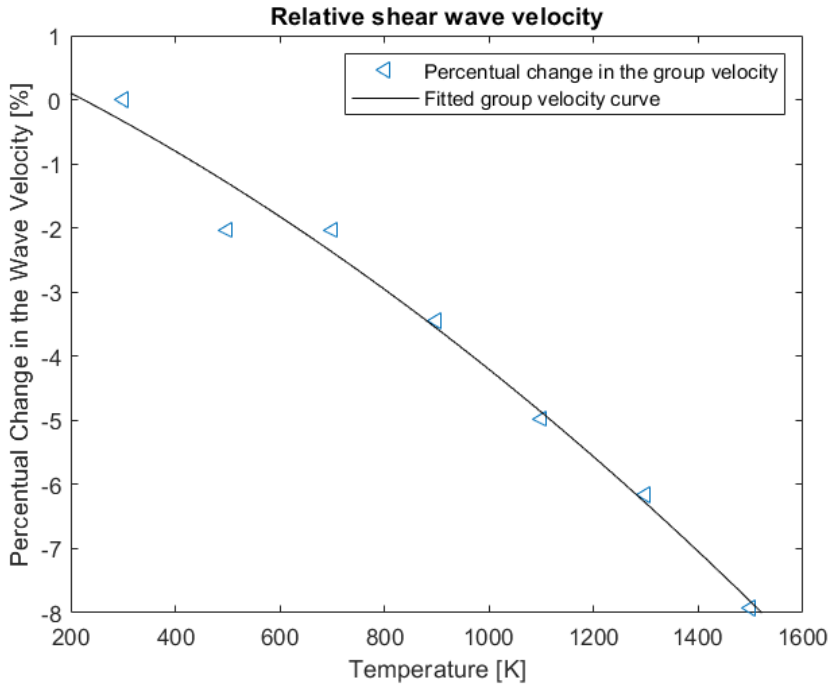

Figure 41: The relative change in group velocity of the shear waves over temperature.

This relative change in group velocity with temperature shows semi-linear behaviour, similar to the longitudinal waves. The group velocity decreases about 8% over a temperature range of $1300K$, similar to both the flexural and longitudinal wave modes. In the operational regime of an MSFR (around $1000K$) the group velocity of shear waves has decreased by about 5% as compared to room temperature. For the derivation of the attenuation of shear wave modes the same maxima are considered as for the velocity derivation (see Figure 36), which were implemented in equation 17. These results are displayed in Figure 42.

The attenuation as measured by the top and the bottom probe do not differ by much (only $3Np/m$), denoting the limited influence of dispersion on the shear wave modes. The simple polynomials show a $1Np/m$ increase in the attenuation for the bottom probe (more disperse regime) and a $2Np/m$ increase in the attenuation for the top probe (less disperse regime), both over a temperature difference of $1300K$. This small increase in attenuation indicates the shear wave modes to be the least temperature dependent (attenuation wise) of all three wave modes. To display this small change even better, the relative changes in the attenuation caused by the temperature are shown in Figure 43.

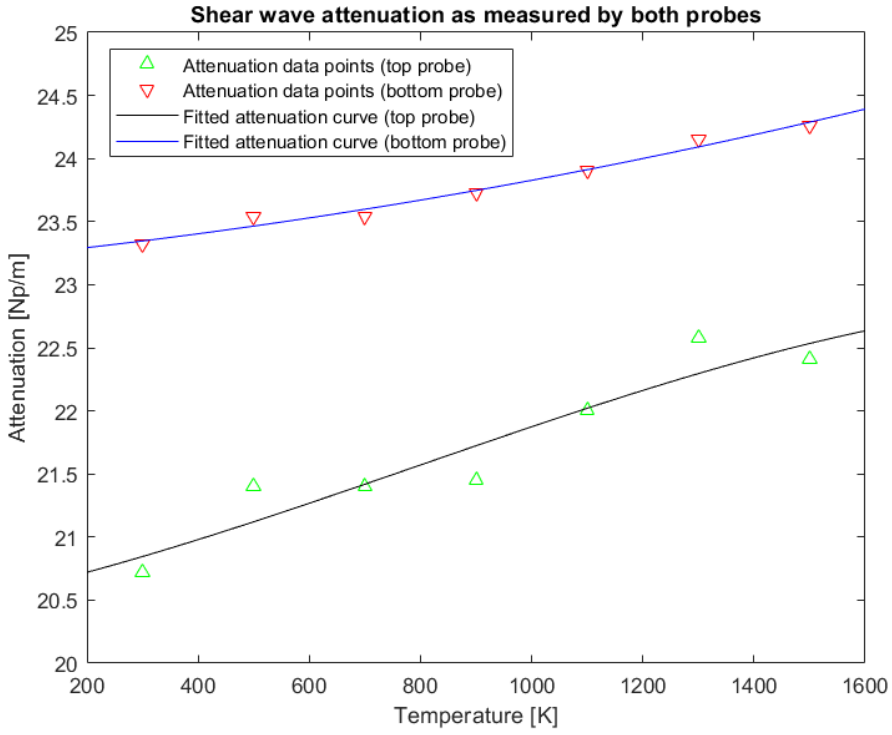

Figure 42: The temperature dependency of the attenuation as measured by the top probe (black curve) and bottom probe (blue curve).

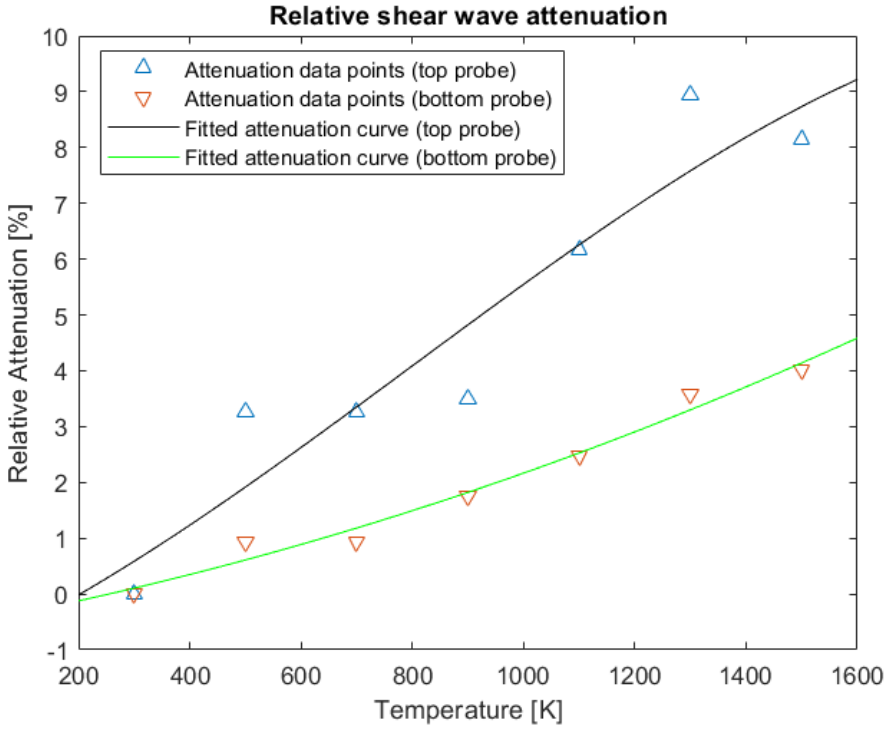

Figure 43: The relative temperature dependency of the attenuation as measured by the top probe (black curve) and bottom probe (green curve).

The percentual changes of the attenuation are similar to the flexural and longitudinal waves with an 8% increase in the attenuation in the non-dispersive regime and a 3% increase in the dispersive regime over a difference in temperature of $1300K$. From the results of the shear waves it can be concluded that shear wave modes are a good option for the intended molten salt experiments. The shear waves show little dispersion and the trailing echoes do not interfere with the main wavefront. Furthermore relatively low absolute values of attenuation were found (around $20Np/m$), which is twice as less as for the longitudinal and flexural wave modes. The group velocity was seen to decrease by around 4% with an increase in temperature from room temperature to operational temperatures of an MSFR. The attenuation increases semi-linearly with only small amounts, but because the attenuation is already small itself, this still gives rise to an increase of about 5%, considering the same temperature range. Temperature dependencies of the attenuation were shown to be less strong for shear waves than for the other two primary wave modes. As stated before, the used data points can be found in *Appendix I: Velocity and attenuation results*.

4.4 Comparison with experimental results

In the real life experiment a transducer excited a heavily distorted signal, seen in Figure 17, through a plate-like waveguide made out of tungsten with dimensions 120 by 80 by 0.2 mm. The transducer measured the signal twice after excitation at the top boundary. At the bottom boundary no physical probe existed. Another difference, next to the different dimensions and input pulse, is the width of the transducer boundary. In the simulations the predescribed displacement (the creation of the pulse) happened along the whole width of the top boundary, and the probing was done using the width of the whole boundary as well. In the real life experiment the transducer only covered a small part of the top boundary, see Figure 3, so the creation of the ultrasonic wave and the measurement of any echoes only happened at this small part of the upper boundary. The tungsten plate was heated with a heat gun until the top of the plate reached a temperature of $313K$. Higher temperatures were not explored to avoid damaging the piezo-electric transducer. The temperature was measured making use of two thermocouples at the top (near the transducer) and the bottom of the waveguide. The considered measurements are shown in Table 2.

Table 2: Considered temperatures used in the real life experiment

	#1	#2	#3	#4
Top Temperature [K]	303	306	310	313
Bottom Temperature [K]	313	323	333	343

The top and bottom temperature in Table 2 do not display the maxima and minima of the temperatures but rather the temperature at the top and at the bottom of the waveguide respectively. This gradient in temperature is another difference between the real life experiment and the simulations. The numbers (#) in the table denote the four measurements done in the experiment. The piezo-electric transducer measures the induced current caused by pressure differences (or normal stress), leading to a displacement (or normal strain) in the z direction. During this experiment only longitudinal waves are excited and considered. The received data, with the excited pulse cut off, can be seen in Figure 44.

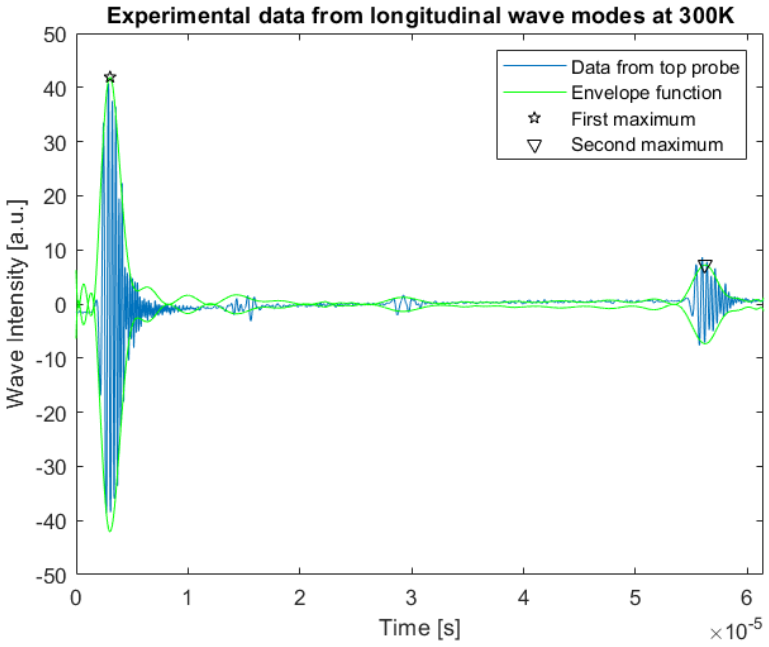

Figure 44: The received longitudinal wave modes from the transducer at the first considered temperature (see Table 2) with the respective envelope function and the maxima shown.

The signal is shown to be noisy and its baseline is slightly offset from zero. The first and second echo can be seen clearly. The offset is due to the heavy amplification of the original pulse (see chapter *3.2: Experimental Set Up*) and disappears when the amplification is tuned back to normal levels. Because of this offset and the noisiness of the signal the original envelope function was shown to be too noisy as well, which caused the maxima location to be erroneous. For that reason a Savitzky-Golay filter was used to smoothen the signal envelope to obtain approximately the right maxima for the velocity and attenuation calculations. To have a first glance at the temperature dependency of the ultrasonic wave behaviour the the lowest and highest temperature considered (see Table 2) were plotted in one graph, seen in Figure 45. From this figure the decrease in wave velocity with an increase in temperature becomes clear, however unlike the simulations the attenuation seems to go down with temperature as well. The variations of the attenuation and velocity as a function of temperature are shown in Figure 46. These calculations were done using the maxima of the first and second echo, as shown in Figure 44 denoted by the star and the downward facing triangle, implemented in formulae 16 and 17 respectively.

A simple first order polynomial was fitted to visualize the results a little better. From these polynomials no qualitative information can be subtracted as they are constructed with little data points, showing great uncertainty. These polynomials only serve the purpose of indicating temperature dependent behaviour. It can be seen that the group velocity drops by 0.3% over a temperature range of $30K$. This shows good agreement with the numerical velocity results of the simulations using the longitudinal wave modes. The velocities measured in the real life experiment are in the order of $4500m/s$, similar to the obtained group velocities from the simulations, also much lower than the literature longitudinal wave velocities of Rose [16] and Nazarchuck [25] of about $5100m/s$. This validates the results obtained from the simulations even more.

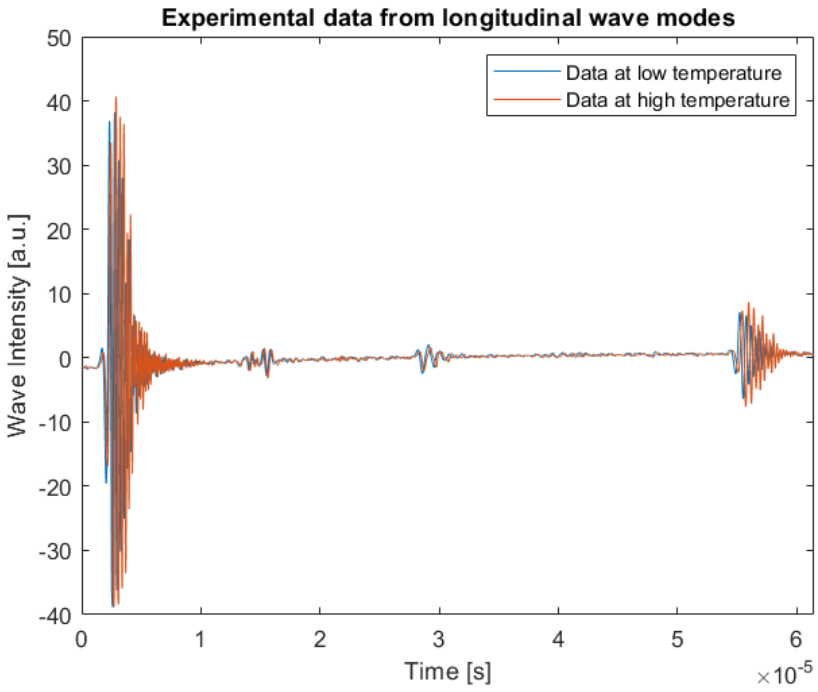

Figure 45: The received longitudinal waves by the transducer at the lowest (blue) temperature and the hottest (red) temperature.

The attenuation results from the experiment differ significantly from the results of the simulations. The attenuation is considerably lower and seems to drop with temperature, whereas the attenuation obtained from the simulations seems to rise with temperature. The absolute difference in attenuation can be assigned to the fact that a stronger pulse was excited to obtain data at the transducer, as such a piezo-electric transducer picks up noise which can make small signals indistinguishable from the noise. Another cause of the lower values of the attenuation is the fact that a $3.5MHz$ pulse was used in the experiment in comparison to the $2MHz$ pulse used in the simulations. As Papadikis [19] showed, higher frequency waves show lower attenuation values. This frequency dependent behaviour can be linked to the dispersion dependent behaviour if energy densities are considered. A high-frequency wave, just like a non-disperse wave, has a high energy density and shows low attenuation. A low-frequency wave, just like a disperse wave, has a low energy density and shows low attenuation. The higher the energy density of the wave package is, the lower the attenuation values will be. A last error-inducing factor could be that, compared to the simulations, the temperature range considered in the experiment is extremely narrow. At such a small part of the temperature spectrum the curves, obtained from the simulations, for the temperature dependence of the attenuation of longitudinal waves can be considered linear and straight (zero slope). The found data from the experiment could resemble this zero-slope linear curve as the uncertainty of the results of the experiment is considerable, due to reasons previously stated.

The shape of the attenuation curve shows differences with the simulation results as well as the attenuation curve of the experiment goes down with temperature and the attenuation curve of the simulations goes up with temperature. This difference is assigned to the noisiness of the signal alongside with the execution of the experiment. The noisiness of the

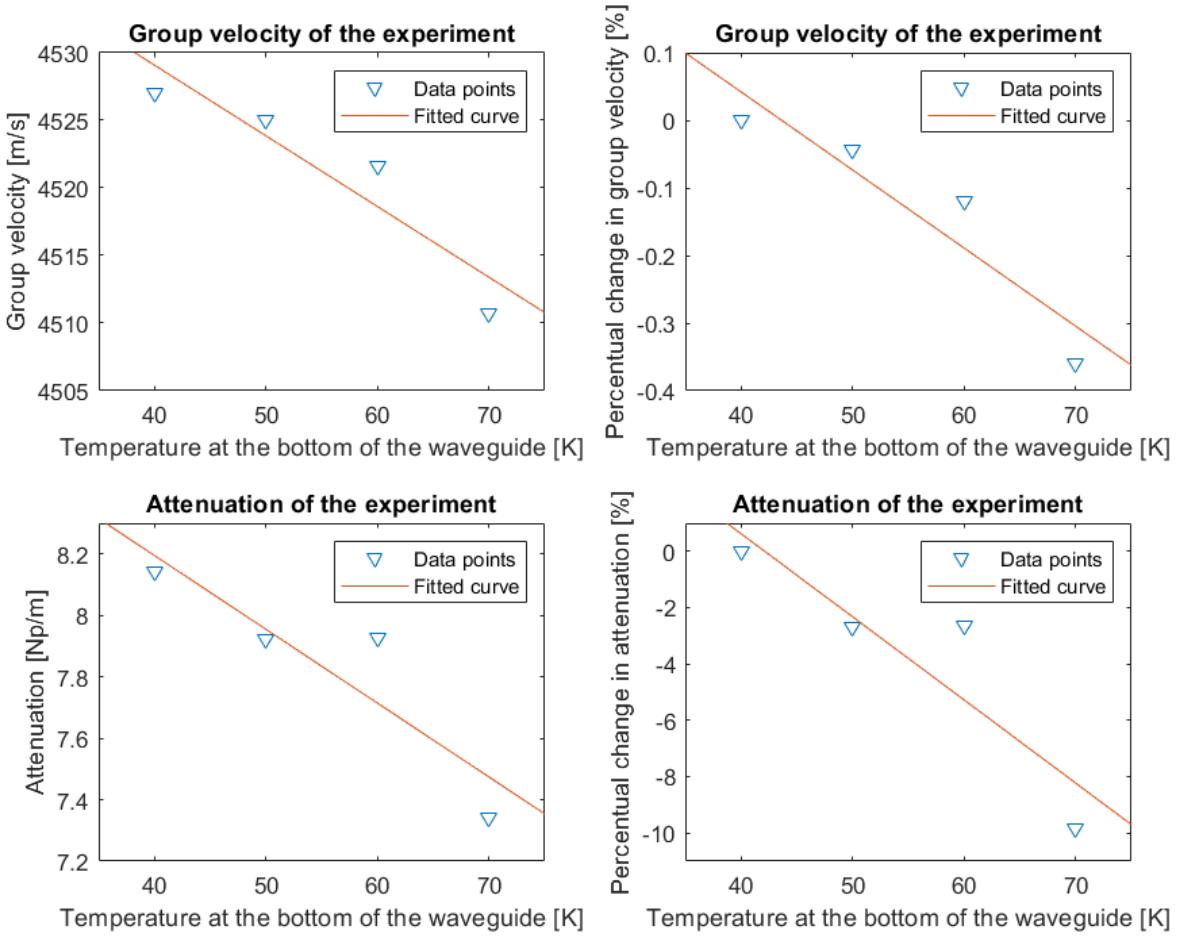

Figure 46: Top left: the absolute change in velocity due to the change in temperature. Bottom left: the absolute change in the attenuation due to the change in temperature. Top right: the relative change in the velocity due to the change in temperature. Bottom right: the relative change in the attenuation due to the change in temperature. On the x-axes the temperature at the bottom of the waveguide is displayed, the corresponding temperature at the top of the waveguide can be found in Table 2. All wave modes considered are longitudinal wave modes.

signal was primarily caused by the high amplification, without the use of electronic amplifiers, of the original pulse. Due to this noisy signal the envelope function, even when filtered, does not 100% correctly display the wave packages. The execution of the experiment was done by aiming a heat gun at the bottom of the waveguide (to prevent damaging the transducer) and recording data as the waveguide warms up. This way a temperature gradient in the waveguide was created and the waveguide did not have time to acclimate to the new temperature. These two error factors explain the deviation in temperature dependent behaviour of the attenuation in the experiment as compared to the behaviour for longitudinal ultrasonic wave attenuation found in the simulations.

The reasons that the recorded wave (Figure 44) shows little similarities to the recorded wave of the simulations (Figure 20) are the different experimental conditions. The excited pulse itself differed from the 5-cycle Hanning used in the simulations, which ultimately resulted in differing data. Furthermore, as mentioned before in the experiment only a small portion

of the upper boundary was excited and recorded the wave, which is thought to have a big influence on the signal (this is going to be one of the follow up researches within this group). The lack of dispersion shown in the experimental data, as compared to the simulation data, even though longer distances are traversed, can be assigned to this fact as well. It was attempted to simulate this exact experiment to overlay the results. This means changing the top boundary probe to only a small part of the boundary, having bigger waveguide dimensions, changing the predescribed displacement to the pulse shown in Figure 17, and creating a temperature gradient. However due to the bigger waveguide size and the need for at least eight mesh elements per wavelength an enormous amount of voxels needed to be created. The computation time of a simulation of that size lies beyond the scope of this research.

4.5 Comparison with literature

The found group velocities have already been compared with literature. The group velocities of the shear and longitudinal wave modes deviated significantly from the literature values found in Nazarchuck [25] and Rose [16]. Nazarchuck and Rose do not state at which temperatures the velocities are measured which can explain the deviation if this was done at lower temperatures than the ones considered in this research. Another cause could lie in the frequency dependence of the group velocity (as already shown by Fuzesi et al. [27]). Relatively low frequencies are used in the simulations and the experiment ($2MHz$ and $3.5MHz$ respectively). The group velocities in Nazarchuck and Rose could have been obtained using higher frequency pulses, which can explain the deviation.

The temperature dependence of wave velocity and attenuation in the high temperature range has not been researched thoroughly. Papadikis is one of the only researchers having done research comparable with the research done in this report. In the work of Papadikis SAE S52100 steel was used in stead of tungsten. Because attenuation and wave velocity in steel differ from those in tungsten those values can not be compared, but the shape of the temperature dependent behaviour can be compared. The shapes of the temperature dependent behaviour of all wave modes are in good agreement. In the work op Papadikis the group velocity however takes a plummet around $1100K$ caused by, according to Papadikis, the change of the crystal structure of the steel from body centered cubic to face centered cubic. The temperature for which this happens for pure tungsten is not widely investigated but one can assume this will happen around $3000K$ as all properties of tungsten (e.g. melting and boiling points) are about thrice as high as those for SAE S52100 steel. Around $3000K$ the group velocities of all wave modes are expected to drop significantly, but this is way outside the considered temperature range for this kind of research, focusing on the MFSR.

The attenuation curves of the shear waves obtained in this research are in good agreement with the ones found in Papadikis for SAE S52100 steel. The attenuation curves for longitudinal waves however differs significantly. Reasons for this variation are attributed to dispersion and the differences between steel and tungsten. Relevant differences could be the magnetization, crystalline transformation, or the solubility of carbides [19]. Another cause could be the equipment used by Papadikis, as the simulations were run in an idealized environment.

4.6 Discussion

The decrease in velocity with an increase in temperature is to be expected. Less dense materials show a significantly lower velocity of ultrasonic waves than materials with a high density. As a warmer metal is less dense and more easily bendable than the same metal at room temperature waves propagate more difficultly. In fact the individual atoms of the metal are not precisely packed but rather resonating and being in motion, as they have more energy at higher temperatures. This results in a lower wave velocity at higher temperatures for all wave modes. The longitudinal wave modes were shown to have a decrease in velocity of $\sim 300m/s$ ($\sim 8\%$) and the flexural waves decreased their velocity by $\sim 150m/s$ ($\sim 7\%$), both over $1400K$. The shear waves showed a decrease in velocity by $\sim 200m/s$ ($\sim 8\%$) over a temperature increase of $1300K$. One could conclude that the group velocities of all wave modes show relative equal temperature dependency.

The attenuation of all wave modes were shown to generally increase with temperature. This is expected as attenuation is (partially) caused by phonon-phonon interactions [28], and phonon-phonon interactions become more dominant at higher temperatures, which results in more attenuation at higher temperatures. The longitudinal waves were shown to have an increase in attenuation of about $4Np/m$ over $1400K$. The flexural wave modes experienced an increase in attenuation of $10Np/m$ over $1200K$ and attenuation of the shear waves increased by $2Np/m$ over $1300K$. The dispersion of the wave modes influenced the attenuation enormously, which resulted generally in higher attenuation values in more disperse regimes. Temperature dependent behaviour of the attenuation is influenced by the dispersion as well, as more disperse wave modes are less influenced by a change in temperature. The (absolute) attenuation of the flexural wave modes was shown to be the highest, which is to be expected as those waves excite the most displacement and deformation within the waveguide, followed closely by longitudinal waves. Shear waves showed the least amount of attenuation. This could be beneficial for the intended molten salt experiments as flexural and longitudinal waves could be completely attenuated when the molten salt is added, where shear waves are likely to "survive" the round trip through the molten salt. In addition to having the lowest overall attenuation shear wave modes also show the smallest increase in attenuation with a rise in temperature of all wave modes.

The results from the real life experiment showed some deviations from the results of the simulations (lower attenuation, different attenuation curves, and less disperse longitudinal wave modes). Those differences are attributed to the difference in the transducer used in the experiment and the boundary probes (one of which executed predescribed displacement), the noisiness of the signal, the heavily distorted input pulse, and frequency dependent behaviour of the attenuation. The frequency dependence of the attenuation (and also the velocity) should be investigated further as this can influence results significantly (as already shown by Cegla [5], Papadikis [19], and Fuzesi [27]. Therefore the results mentioned in this report are only valid for pulses of $2MHz$. The influence of a small transducer instead of a whole boundary is being researched right now in our group.

Another aim of this research was to investigate the negligibility of the physical thermal expansion and hardening of the tungsten waveguide. These simulations however showed non-physical results and a convergence study showed that for these results to be physical the voxel size should be decreased significantly. This would result in computation times and file sizes way beyond the scope of this research. This could be an area for follow up research.

This research gives a broad understanding of the temperature dependent behaviour of the attenuation and the group velocity of the three primary wave modes. For a more detailed understanding of this temperature dependent behaviour the same study needs to be done with smaller steps in temperature. With the focus on the MSFR many temperatures should be considered around room temperature and the operational temperature of the desired MSFR (around $1000K$) to give a good understanding of the relation between the prototype experiment and the desired molten salt experiments. Another interesting temperature that can be considered in future experiments would be around $1300K$, considering flexural waves, where unexpected behaviour has occurred. Furthermore, as already mentioned, the frequency dependent behaviour for all wave modes is an interesting research area.

5 Conclusions and recommendations

5.1 Conclusions

The goal of this research was to explore the temperature dependent behaviour of the attenuation and velocity of ultrasonic wave modes (longitudinal, flexural, and shear) through a tungsten waveguide over a broad temperature range. The longitudinal and shear wave modes were found to show a semi-linear decrease in velocity and increase in attenuation over a temperature spectrum of $1400K$. The temperature dependent behaviour of the flexural wave modes was found to be more complex.

Disperse effects and additional wave modes were shown to have great impact on the attenuation of the ultrasonic waves. Longitudinal waves were shown to have the most dispersion and were influenced greatly by additional wave modes, which caused the attenuation derivation to be more difficult. Flexural and shear waves were found to show acceptable levels of dispersion and interference with additional wave modes.

If the temperature is increased from room temperature ($\sim 300K$) to operational temperatures of an MSFR ($\sim 1000K$) the longitudinal waves showed a decrease in velocity of $200m/s$ (3%) and the flexural and shear waves both dropped their velocity by $100m/s$ (5%). Over the same temperature range the attenuation of longitudinal waves was seen to increase by $2Np/m$. The increase in attenuation for the flexural and shear waves depended on the degree of dispersion shown by the waves. In the non-disperse regime flexural waves increased their attenuation by $12Np/m$ (15%) and in the disperse regime the attenuation increased by $6Np/m$ (10%). The non-disperse shear waves showed and increase in attenuation of $1Np/m$ (5%) and when the waves experienced any dispersion the attenuation increased by less than $1Np/m$ (1%). This decrease in attenuation-increase in highly-disperse regimes is due to the energy of a wave mode being more spread out over the whole wave package and additional wave modes.

In general the shear waves seem to be the best fit for intended ultrasonic measurements to derive properties of a molten salt. The longitudinal and flexural wave modes showed a high amount of attenuation ($\sim 50Np/m$) and it is to be expected that if a molten salt is added these wave modes attenuate even more, up to the point that no information can be derived from the echoes of the wave. On top of that longitudinal wave modes showed a problematic amount of dispersion and interfering additional wave modes. The shear wave modes did show the creation of additional wave modes, but these were proven to be non-problematic. The absolute attenuation values of the shear wave modes were about $20Np/m$ and only increased about $1Np/m$ if the temperature is increased from room temperature to operational temperatures of an MSFR. Both the velocity and attenuation temperature dependent curves were found to be semi-linear and predictable. Even though the temperature induced change in attenuation and velocity is relatively small for the shear waves, this change cannot be neglected if qualitative and precise measurements are desired.

For this reason more extensive research within this field is desired investigating more temperatures around room temperature operational temperatures of an MSFR.

5.2 Recommendations

It is recommended to investigate all wave modes at a denser variety of temperatures, as in this research only seven temperatures were considered. With the focus on intended molten salt experiments it is recommended to investigate the behaviour of shear waves, as they are the best fit, in temperatures close to room temperature and temperatures close to operational temperatures of an MSFR. This way a test experiment at room temperature can be easily scaled towards actual measurements using molten salts.

Secondly the influence a temperature gradient has on the behaviour of the ultrasonic waves is an interesting area for follow up research. In this research only constant temperatures were considered, where in the intended molten salt experiment a temperature gradient will be present.

Another recommendation is to investigate the frequency dependence of the attenuation and velocity for different wave modes, as earlier research showed that the frequency does influence the attenuation and wave velocity. Therefore this research is only valid for $2MHz$ pulses until extensive research has been performed to qualitatively couple wave behaviour at different frequencies.

Furthermore the influence of a transducer, as compared to the excitation and probing of a whole boundary, is a recommended area for follow up research. The experiment has shown that this influence is not to be neglected. As a last recommendation the influence of thermal expansion and hardening can be explored. In this research tungsten was assumed to be perfectly elastic, which is an idealization. The influence of such inelastic behaviour is expected to be negligible, but for completeness this is an interesting area for follow up research.

References

[1] E. S. Bettis, W. B. Cottrell, E. R. Mann, J. L. Meem, and G. D. Whitman. The aircraft reactor experiment-operation. *Nuclear Science and Engineering*, 2(1):841–853, June 1957.

[2] Elisa Capelli. *Thermodynamic Characterization of Salt Components for Molten Salt Reactor Fuel*. PhD thesis, Delft University of Technology, Mekelweg 2, 2628 CD, Delft, February 2016.

[3] Ian R. Scott and John Durham. The simple molten salt reactor, practical, safe and cheap. In *Moltex Energy LLP*, 2018.

[4] W.R. Grimes. Molten-salt reactor chemistry. *Nuclear Applications and Technology*, 8:137–155, February 1970. Oak Ridge National Laboraory, Oak Ridge, Tennessee 37830.

[5] F.B. Cegla, P. Cawley, and M.J.S. Lowe. Material property measurement using the quasi-scholte mode — a waveguide sensor. *Acoustical Society*, 43(35.Mr):1098–1107, November 2004. Department of Mechanical Engineering, Imperial College London, London SW7 2AZ, United Kingdom.

[6] F.B. Cegla, P. Cawley, and M.J.S. Lowe. Fluid bulk velocity and attenuation measurements in non-newtonian liquids using a dipstick sensor. *Measurement Science and Technology, Institute of Physics Publishing*, 17(264):264–274, December 2005. Department of Mechanical Engineering, Imperial College London, London SW7 2AZ, UK.

[7] Frédéric Bert Cegla. *Ultrasonic Waveguide Sensors for Fluid Characterisation and Remote Sensing*. PhD thesis, Department of Mechanical Engineering, Imperial College London, London SW7 2BX, January 2006.

[8] T. Stevenson, D. G. Martin, P.I. Cowin, A. Blumfield, A.J. Bell, T. P. Comyn, and P.M. Weaver. Piezoelectric materials for high temperature transducers and actuators. *J Mater Sci: Mater Electron*, 26:9256–9267, August 2015.

[9] H. A. J. Froeling. Causes of spurious echoes by ultrasonic wave simulation. Bachelor of science thesis, Delft University of Technology, June 2017.

[10] T.S. Oud. Elastic wave simulation for buffer rod tapering. Bachelor of science thesis, Delft University of Technology, August 2017.

[11] Sara Mastromarino. Progress Report, February 2018.

[12] Marc van den Berg. High temperature viscosity determination using the quasi-scholte wave. Progress Report, March 2018.

[13] Olivier Schuringa. Density and viscosity calculation using ultrasonic wave propagation. Bachelor of science thesis, Delft University of Technology, December 2017.

[14] COMSOL Multiphysics® version 5.3. Software. COMSOL AB, Stockholm, Sweden, December 2017.

[15] MATLAB® version R2018a. Software. MathWorks, Natick, Massachusetts, United States, March 2018.

[16] Joseph L. Rose. *Ultrasonic Guided Waves in Solid Media*. Cambridge University Press, 32 Avenue of the Americas, New York NY, 10013-2473, USA, 2014.

[17] M. Korolczuk-Hejnak, P. Migas, and W. Slezak. Determination of the liquid steel viscosity curves using a high temperature rheometer. *Journal of Physics: Conference Series*, 602, January 2015.

[18] Alan V. Oppenheim, Alan S. Willsky, and S. Hamid Nawab. *Signals and Systems*. Prentice-Hall International, Inc, 1983.

[19] Emmanuel P. Papadikis, Lawrence C. Lynnworth, Kenneth A. Fowler, and Edmund H. Carnevale. Ultrasonic attenuation and velocity in hot speciments by the momentary contact method with pressure coupling, and some results on steel to 1200c. *The Journal of the Acoustical Society of America*, 52(3):850–857, September 1971.

[20] L. Binkele. Zur frage der hochtemperatur-lorenzzahl bei wolfram - eine analyse neuer messwerte der thermischen und elektrischen leitfaehigkeit im temperaturbereich 300 bis 1300 k. *High Temperatures - High Pressures*, 15:525–531, May 1983.

[21] Peter Hidnert and W.T. Sweeney. Thermal expansion of tungsten. *Scientific Papers of the Bureau of Standards*, 20(S515):483–486, August 1925.

[22] S. Yadav and K.T. Ramesh. The mechanical properties of tungsten-based composites at very high strain rates. *Elsevier Science S.A.*, A203:140–153, May 1995.

[23] L. P. B. M. Janssen and M. M. C. G. Warmoeskerken. *Transport Phenomena Data Companion*. Delft Academic Press, Leeghwaterstraat 42, 2628 CA Delft, the Netherlands, 1987.

[24] LabVIEW® version 2017. Software. National Instruments, Austin, Texas, United States, May 2017.

[25] Z. Nazarchuck et al. Acoustic emission. *Foundations of Engineering Mechanics*, 1007/978-3-319-49350-3_2:29–73, October 2017.

[26] B.K. Basu. Ultrasonic attenuation in nickel in the vicinity of curie temperature. *Basic Solid State Physics*, 38(2):857–863, October 1970.

[27] Krisztian Fuzesi, Natalia Ilyina, Erik Verboven, Koen van den Abeele, Miklos Gyongy, and Jan Dhooge. Temperature dependence of speed of sound and attenuation of procine left ventricular myocardium. *Ultrasonics*, 82:246–251, January 2018.

[28] S. D. Lambade, G. G. Sahasrabudhe, and S. Rajagopalan. Temperature dependence of acoustic attenuation in silicon. *Physical Review B*, 51(22):15861–15866, June 1995.

A Appendix I: Velocity and attenuation results

Longitudinal waves

Table 3: Table containing all of the data used in this report for longitudinal waves.

Quantity	300K	500K	700K	900K	1100K	1300K	1500K
Velocity [m/s]	4478	4445	4396	4356	4301	4248	4196
Attenuation (Top) [Np/m]	10.00	10.54	10.93	11.33	11.95	12.83	13.64
Attenuation (Bottom) [Np/m]	48.89	48.98	49.43	50.15	50.57	51.29	51.96

Flexural waves

Table 4: Table containing all of the data used in this report for flexural waves.

Quantity	300K	500K	700K	900K	1100K	1300K	1500K
Velocity [m/s]	2007	1966	1946	1924	1904	1927	1868
Attenuation (Top) [Np/m]	40.10	44.19	44.58	45.12	45.67	43,29	47,77
Attenuation (Bottom) [Np/m]	48.06	55.55	55.90	56.62	57.55	50.82	59.14

Shear waves

Table 5: Table containing all of the data used in this report for shear waves.

Quantity	300K	500K	700K	900K	1100K	1300K	1500K
Velocity [m/s]	2720	2665	2665	2627	2585	2553	2505
Attenuation (Top) [Np/m]	20.72	21.40	21.40	21.45	22.00	22.58	22.41
Attenuation (Bottom) [Np/m]	23.32	23.54	23.54	23.73	23.90	24.15	24.26

B Appendix II: Parameters used in COMSOL Multiphysics

Longitudinal and flexural wave modes

Table 6: Table containing all the parameters used in the simulations for longitudinal and flexural waves.

Parameter	Expression	Unit	Description
Ap	1e-10	-	Pulse amplitude
c_long	5180 [25]	m/s	Longitudinal wave velocity
c_shear	2870 [25]	m/s	Shear wave velocity
c_trans	2650 [25]	m/s	Flexural wave velocity
D	0.1	mm	Depth of the plate
Ny	100	-	Minimal amount of data points per pulse
f0	2	MHz	Frequency of the pulse
Abscissa	W*N*labda_c_shear	-	Minimal amount of mesh elements (x)
Ordinate	D*N*labda_c_trans	-	Minimal amount of mesh elements (y)
Applicate	L*N*labda_c_long	-	Minimal amount of mesh elements (z)
L	1.2	cm	Length of the plate
labda_c_long	c_long/f0	m	P-wave wavelength
labda_c_shear	c_shear/f0	m	S-wave wavelength
labda_c_trans	c_trans	m	Flexural wave wavelength
MES	D/100	m	Minimal mesh element size
N	8	-	Minimal mesh elements per wavelength
T	Varies from 300 to 1500	K	Temperature
t_end	4/f0	s	End time of the pulse
t_limit	2500*t_step	s	End time of the simulation
t_step	t_end/dat	s	Maximum time step taken
W	L/2	m	Width of the plate

Shear wave modes

Table 7: Table containing all the parameters used in the simulations for shear waves.

Parameter	Expression	Unit	Description
Ap	1e-10	-	Pulse amplitude
c_long	5180 [25]	m/s	Longitudinal wave velocity
c_shear	2870 [25]	m/s	Shear wave velocity
c_trans	2650 [25]	m/s	Flexural wave velocity
D	0.1	mm	Depth of the plate
Ny	100	-	Minimal amount of data points per pulse
f0	2	MHz	Frequency of the pulse
Abscissa	W*N*labda_c_shear	-	Minimal amount of mesh elements (x)
Ordinate	D*N*labda_c_trans	-	Minimal amount of mesh elements (y)
Applicate	L*N*labda_c_long	-	Minimal amount of mesh elements (z)
L	4	cm	Length of the plate
labda_c_long	c_long/f0	m	P-wave wavelength
labda_c_shear	c_shear/f0	m	S-wave wavelength
labda_c_trans	c_trans	m	Flexural wave wavelength
MES	D/100	m	Minimal mesh element size
N	8	-	Minimal mesh elements per wavelength
T	Varies from 300 to 1500	K	Temperature
t_end	4/f0	s	End time of the pulse
t_limit	2500*t_step	s	End time of the simulation
t_step	t_end/dat	s	Maximum time step taken
W	L/2	m	Width of the plate